



Looking beyond kinematics: 3D thermo-mechanical modelling reveals the dynamic of transform margins

Anthony Jourdon¹, Charlie Kergaravat¹, Guillaume Duclaux², Caroline Huguen¹

1- Research & Development, Total S.A., Pau, France

2- Université Côte d'Azur, CNRS, Observatoire de la Côte d'Azur, IRD, Géoazur, France

Correspondence to: Anthony Jourdon (jourdon.anthon@gmail.com)

Abstract

Transform margins represent ~30% of the non-convergent margins worldwide. Their formation and evolution have long been addressed through kinematic models that do not account for the mechanical behaviour of the lithosphere. In this study, we use high resolution 3D numerical thermo-mechanical modelling to simulate and investigate the evolution of the intra-continental strain localization under oblique extension. The obliquity is set through velocity boundary conditions that range from 15° (high obliquity) to 75° (low obliquity) every 15° for strong and weak lower continental crust rheologies. Numerical models show that the formation of localized strike-slip shear zones leading to transform continental margins always follows a thinning phase during which the lithosphere is thermally and mechanically weakened. For low (75°) to intermediate (45°) obliquity cases, the strike-slip faults are not parallel to the extension direction but form an angle of 20° to 40° with the plates' motion while for higher obliquities (30° to 15°) the strike-slip faults develop parallel to the extension direction. Numerical models also show that during the thinning of the lithosphere, the stress and strain re-orient while boundary conditions are kept constant. This evolution, due to the weakening of the lithosphere, leads to a strain localization process in three major phases: (1) strain initiates in a rigid plate where structures are sub-perpendicular to the extension direction; (2) distributed deformation with local stress field variations and formation of transtensional and strike-slip structures; (3) formation of highly localized plates boundaries stopping the intra-continental deformation. Our results call for a thorough re-evaluation of the kinematic approach to studying transform margins.

1. Introduction

Transform margins, represent ~30% of the non-convergent margins worldwide (Mercier de Lépinay et al., 2016; Mélody Philippon & Corti, 2016). Transform continental margin refers to the continent-ocean transition derived from a transform plate boundary that accommodates, or has accommodated, ocean spreading (Basile, 2015; Mascle & Blarez, 1987). Transform continental margins are limited by transform faults connected with divergent margins at both ends. In contrast with continental passive margins, continental transform margins have received limited attention, probably due of their non-cylindrical nature and the steep geometry of the deformed structures that make difficult their imaging by reflection seismic.

Kinematic interpretations of transform margins are mainly based on a conceptual model (Basile, 2015; Basile et al., 2013; Mascle & Blarez, 1987; Scrutton, 1979). This conceptual model was first



39 established from seismic lines interpretations along the conjugate Equatorial Atlantic margins (Fig. 1)
40 assuming inherited plate boundaries (Mascle & Blarez, 1987). It then became more widely used and
41 applied to other plate margins around the world such as the South African margin (Parsiegla et al.,
42 2009), the Antarctic Southern Exmouth Plateau along the South Australian margin (Lorenzo & Vera,
43 1992), the West Greenland margin (Suckro et al., 2013). This original conceptual model involves the
44 formation of offset intra-continental rift segments linked by a transform fault since the early stages of
45 extension. As a consequence, the whole rift-transform fault system evolves synchronously during
46 continental thinning and oceanic accretion. The onset of oceanic accretion marks the start of the triple
47 junction migration along the transform margin at half the spreading velocity (Basile, 2015; Gerya,
48 2012). The transform continental margin is then considered active during the migration of the oceanic
49 accretion axis along the continental domain. Whether transform faults originate pre- or syn-rifting or
50 even post-continental break-up is still a matter of debate. More recently, based on natural examples,
51 Bellahsen et al. (2013) and Basile (2015) highlighted that transform faults can form either
52 synchronously with the syn-rift structures and may reactivated or cross-cut inherited structures (e.g.
53 Equatorial Atlantic; Gulf of California, Fig. 1), or develop after the oceanic spreading starts, to
54 connect offset oceanic ridges (e.g. Woodlark basin e.g. Taylor et al., 2009).

55 This conceptual model and its offspring based on rigid plate tectonics does not reflect the whole intra-
56 continental deformation phase associated with progressive strain localization and structures re-
57 orientation (Ammann et al., 2017; Brune, 2014; Brune & Autin, 2013; Mondy et al., 2018; Le Pourhiet
58 et al., 2017). This has first order implications on tectonic plates reconstruction and the interpretation of
59 margins progressive deformation history. In highly oblique systems, during intra-continental stage, the
60 relative plate motion between two divergent segments is mostly accommodated by strain partitioning
61 along transfer fault zones (Milani & Davison, 1988). In order to better understand the dynamics of
62 such transform margins, from initiation in continental domains to maturity, it is therefore required to
63 account for lithosphere physical properties. Both analogue and numerical modelling studies have
64 focused on the formation and evolution of transform continental margins. Different modelling
65 approaches have been used to investigate parameters that control intra-continental deformation and
66 transform margin formation, all of them implying oblique plate motion (rift obliquity controls the
67 orientation and proportion of normal and strike-slip faults). On the one hand, this obliquity can be
68 either imposed through initial conditions with oblique pre-existing weak zones representing a
69 structural inheritance (Agostini et al., 2009; Ammann et al., 2017; Brune et al., 2012; Corti, 2012;
70 Duclaux et al., 2020; Mart & Dauteuil, 2000; Tron & Brun, 1991) or imposed en-échelon offset weak
71 zones (Allken et al., 2012; Le Calvez & Vendeville, 2002; Liao & Gerya, 2015; Le Pourhiet et al.,
72 2017; Zwaan et al., 2016). On the other hand, obliquity can be set through boundary conditions with
73 oblique extension (Brune, 2014; Brune et al., 2012; Brune & Autin, 2013) or pure shear conditions
74 (Gerya & Burov, 2018; Jourdon et al., 2020; Le Pourhiet et al., 2018) relative to the domain borders.

75 Except in experiments approaching pure strike-slip conditions, models show that the onset of intra-
76 continental deformation always localizes on structures closely orthogonal to the extension direction
77 (e.g. Brune, 2014; Duclaux et al., 2020). Then, depending on the obliquity (defined as the angle
78 between the plate motion direction and the average rift trend) the deformation evolution differs.
79 Resulting rifts systems are generally classified in three categories: (1) low obliquity, (2) intermediate
80 obliquity and (3) high obliquity.

81 Low obliquity systems are close to orthogonal extension. For models with oblique extension or
82 oblique weak zones it represents angles from 60° to 90° between extension direction and weak zones
83 trend. In models involving offset rifts, low obliquity is reached for offsets of 100 km and less (Allken



84 et al., 2012; Liao & Gerya, 2015; Le Pourhiet et al., 2017). In these systems, the deformation is almost
85 always orthogonal to the extension direction and the developing structures are mainly extensional.

86 Intermediate obliquity is reached in models involving an oblique weak zone or oblique extension for
87 angles of extension between 30° and 60° (Agostini et al., 2009; Brune, 2014; Corti, 2012; Duclaux et
88 al., 2020), while for models with offset weak zones, an offset of 100 km to 300 km is required (Le
89 Pourhiet et al., 2017). In this context, once the continental lithosphere thinned enough, the rheology of
90 the whole system evolves and the deformation regime changes to reach transtensional deformation.
91 Large scale strike-slip structures develop to connect isolated rift basins segments and accommodate
92 the obliquity. However, strike-slip structures are not parallel to the extension direction as transform
93 faults are in natural systems.

94 Finally, high obliquity represents systems in which the deformation regime approaches pure strike-slip
95 conditions. These conditions can be reached for obliquities lower than 30° between the rift trend and
96 the extension direction (Agostini et al., 2009; Ammann et al., 2017; Brune, 2014) or offset between
97 rifts larger than 300 km (Le Pourhiet et al., 2017). This highly oblique deformation regime is rarely
98 simulated, due to a strong limitation in models' setups associated with the use of free-slip boundary
99 conditions on the vertical boundaries of the model. Indeed, free-slip boundary conditions that are
100 generally used for vertical boundaries trending parallel to the extension direction physically prevent
101 deformation in the direction normal to the face (i.e. if free-slip is applied to a boundary of normal x , no
102 deformation can occur in x direction along this border). Therefore, models involving oblique or offset
103 weak zones show that in high obliquity contexts two independent rifts develop and never link (Le
104 Pourhiet et al., 2017) suggesting a natural propensity for segmented rifts systems rather than oblique
105 ones. However, this context seems to be the best candidate to form transform faults parallel to the
106 extension direction segmenting two spreading systems. Indeed, Ammann et al., (2017) showed that a
107 transform fault can develop in a highly oblique weak zone forming an angle of 16° with the extension
108 direction if intense softening is applied. This softening is set in their models through low viscosity
109 magmatism, allowing the viscosity in the weak zone to drop of 4 to 6 orders of magnitude compared to
110 the surrounding material.

111 Here we investigate numerically the effect of oblique extension on strain partitioning and localization
112 during early rifting and break-up in the continental lithosphere using non-free slip and oblique
113 boundary conditions and different lower crustal rheologies. We first present high resolution 3D
114 numerical thermo-mechanical models illustrating the evolution of intracontinental rifting processes
115 and strike-slip deformation leading to the formation of transform/strike-slip margins. We then discuss
116 the implication of the crustal rheology on strain localization and strike-slip deformation. Finally, we
117 compare the models' results to emblematic natural examples of transform margins and propose a
118 simplified tectonic evolution model for the formation of transform margins in intermediate and highly
119 oblique extension.

120 **2. Setup for thermo-mechanical numerical modelling**

121 *2.1. Modelling approach and initial conditions*

122 In order to model the long term deformation of the lithosphere we use pTatin3D (May et al., 2014,
123 2015), a highly scalable, massively parallel implementation of the finite element method. It employs
124 an Arbitrary Lagrangian-Eulerian (ALE) discretization together with the material point method to
125 solve the conservation of mass and momentum for an incompressible fluid coupled with energy
126 conservation.



127 The geometry of the modelled domain is 1200 km in the x direction, 600 km in the z direction and
 128 250 km in the vertical y direction (Fig. 2a). Two sets of models are conducted: the first set involves ten
 129 models with a resolution of 512x256x128 elements while the second set involves three high resolution
 130 models of 1024x512x256 elements for a resolution about 1 km x 1 km x 1 km. The initial lithosphere
 131 geometry involves four flat layers. The crust is divided into an upper crust from $y=0$ km to $y=-20$ km
 132 and a lower crust from $y=-20$ km to $y=-40$ km. The upper crust is simulated with a quartz flow law
 133 (Ranalli & Murphy, 1987) when viscous deformation takes place. Since the lower crust rheology is
 134 known to have a first order control on strain localization (Allken et al., 2012; Brune et al., 2017; Corti,
 135 2012; Jourdon et al., 2020; Le Pourhiet et al., 2017) we conducted all the experiments with two
 136 different lower crust rheologies. The “weak” lower crust models involve a quartz flow law (Ranalli &
 137 Murphy, 1987) while the “strong” lower crust models involve an anorthite flow law (Rybacki &
 138 Dresen, 2000). The mantle is also divided into two layers, the lithosphere mantle (from $y=-40$ km to
 139 $y=-120$ km) and the asthenosphere mantle (from $y=-120$ km to $y=-250$ km) that share the same
 140 rheology simulated with an olivine flow law (Hirth & Kohlstedt, 2003). To simulate the brittle parts of
 141 the lithosphere we use the Drucker-Prager pseudo-plastic yield criterion adapted to continuum
 142 mechanics (see equation A5).

143 Table 1: parameters used for the different flow laws in the model

	Units	Quartz	Anorthite	Olivine
Reference		Ranalli and Murphy 1987	Rybacki and Dresen 2000	Hirth and Kohlstedt 2003
A	MPa ⁻ⁿ .s ⁻¹	6.3x10 ⁻⁶	13.4637	1.1x10 ⁵
n		2.4	3	3.5
Q	KJ/mol	156	345	530
V	m ³ .mol ⁻¹	0	3.8x10 ⁻⁵	18x10 ⁻⁶

144

145 The initial temperature field is set with a steady-state analytical solution (Turcotte & Schubert,
 146 2002)

$$147 \quad T_{\text{init}} = T_{y=0} + \frac{-yq_m}{k} + H \frac{y_p^2}{k} \left(1 - \exp\left(\frac{-y}{y_p}\right) \right) \quad (1)$$

148 with $T_{y=0} = 0^\circ\text{C}$, an incoming mantle heat flux $q_m = 20 \text{ mW.m}^{-2}$, a radiogenic heat production $H =$
 149 $1.2 \times 10^{-6} \text{ W.m}^{-3}$, a characteristic radiogenic layer of $y_p = 40 \text{ km}$ and a conductivity of $3.3 \text{ W.m}^{-1}.\text{K}^{-1}$.
 150 With this analytical solution the temperature at the Moho (40 km depth, Fig. 2c) is 610°C and the
 151 lithosphere-asthenosphere boundary (1300°C) lies at 120 km depth (Fig. 2c). Then, from 120 km to
 152 250 km depths we prescribe a linear increase of the temperature representing an adiabatic gradient of
 153 0.5°C/km (Fig. 2c). Although this second part of the geotherm is not at steady state, the cooling by
 154 diffusivity is very slow (less than 2°C/Myr for the maximum cooling rate) and it allows to keep
 155 reasonable conductivity values in the asthenosphere ($3.3 \text{ W.m}^{-1}.\text{K}^{-1}$).

156 The initial radiogenic heat production is set as an exponential decay of heat production with depth
 157 according to Turcotte & Schubert (2002) as follow:

$$158 \quad H = H_0 \exp\left(\frac{-y}{y_p}\right) \quad (2)$$



159 for a surface production H_0 of $1.2 \times 10^{-6} \text{ W.m}^{-3}$.

160 In order to initiate the deformation in the central part of the model we define three weak zones that
161 could represent tectonic inheritances in which we prescribe an initial amount of plastic strain that
162 reduces the friction angle as:

$$163 \quad \varphi = \varphi_0 - \frac{\varepsilon_p - \varepsilon_{\min}}{\varepsilon_{\max} - \varepsilon_{\min}} (\varphi_0 - \varphi_{\infty}) \quad (3)$$

164 Where φ is the friction angle, φ_0 the initial friction angle (30°), φ_{∞} the minimum friction angle
165 (5°), ε_p the plastic strain and ε_{\min} and ε_{\max} the minimum and maximum values of plastic strain between
166 which the plastic strain softening is applied (respectively 0 and 1). The geometry consists in three
167 cubic damaged zone with a side length of 200 km and centred at $x = \{200; 600; 1000\}$ and $z = 300$
168 km.

169 2.2. Boundary conditions

170 The boundary conditions to solve the conservation of momentum are defined with velocity vectors
171 oblique to the boundary (Fig. 2b). On faces normal to the z-axis, we impose the same velocity on the
172 whole face with opposite directions between face z_{\min} and face z_{\max} . On faces normal to the x-axis, we
173 impose periodic boundary conditions (Fig. 2b). The angle of extension α is determined as the angle
174 between the velocity vector and z, the horizontal direction normal to x (Fig. 2b). For every models we
175 impose a velocity vector of norm $\|\vec{v}\| = 0.5 \text{ cm/a}$ on each face. Each component of the velocity vector
176 is therefore computed as:

$$177 \quad \vec{v} = \begin{pmatrix} v_x = \sqrt{\|\vec{v}\|^2 - v_z^2} \\ v_z = \|\vec{v}\| \cos \alpha \end{pmatrix} \quad (4)$$

178 The basal boundary condition is defined as a constant inflow to compensate the outflow as:

$$179 \quad v_y = \frac{2\|\vec{v}\|.L_x.L_y}{L_x.L_z} \quad (5)$$

180 Where L_x , L_y and L_z are the length of the domain in the corresponding direction.

181 The boundary conditions to solve the conservation of energy are null heat fluxes on vertical
182 boundaries, $T_{y=0} = 0^\circ\text{C}$ and $T_{y=\text{bottom}} = 1365^\circ\text{C}$.

183 3. Post-processing

184 In order to best interpret the tectonic evolution of the oblique rift models we choose to represent the
185 stress inferred deformation regime, the finite strain and the beta factor in map views. We also display
186 cross-sections oriented either perpendicularly to the strike-slip structures or to the extensional ones on
187 which the second invariant of the strain rate tensor is computed as follow:

$$188 \quad \dot{\varepsilon} = \frac{1}{2} (\nabla \vec{v} + \nabla \vec{v}^T) \quad (6)$$

189 Where $\dot{\varepsilon}$ is strain rate tensor and v the velocity vector. The second invariant is then computed as:

$$190 \quad \dot{\varepsilon}^{II} = \sqrt{\frac{1}{2} \dot{\varepsilon}_{ij} \dot{\varepsilon}_{ij}} \quad (7)$$

191 With the Einstein summation convention.



192 The stress inferred deformation regime is used to determine which is the dominant instantaneous
 193 deformation regime knowing as extensional, transtensional, strike-slip, transpressional and
 194 compressional. This method has been used in several studies (Brune, 2014; Brune & Autin, 2013;
 195 Buchmann & Connolly, 2007; Delvaux et al., 1997; Hergert & Heidbach, 2011; Simpson, 1997) and
 196 allows better interpreting the active tectonic structures. The detailed method is well expressed in
 197 Brune et al. 2014 in order to compute the regime stress ratio (RSR) giving a scalar ranging from 0 to 3
 198 corresponding to a continuous evolution from extension, transtension, strike-slip, transpression and
 199 compression. On Figures 3, 5, 7 we represented each of these deformation regimes with different
 200 colours. The following table 2 displays the upper and lower bounds of each deformation regime.

201 Table 2: Regime Stress Ratio (RSR) values and corresponding interpretation

RSR value	Strain regime
0 – 0.75	Extension
0.75 – 1.25	Transtension
1.25 – 1.75	Strike-slip
1.75 – 2.25	Transpression
2.25 – 3.0	Compression

202

203 The maps of finite strain (Fig. 3, 5, 7) display both plastic strain and the mantle exhumation age when
 204 the mantle starts to exhume. The plastic strain is computed as the cumulative deformation over time
 205 when deformation occurs under the Drucker-Prager yield criterion (eq. A6). The mantle exhumation
 206 age is designed to be compared with oceanic seafloor age or magnetic anomalies. It is computed as the
 207 time at which the particles cooled down below 800°C (Jourdon et al., 2020).

208 On Figures 3, 5, 7, the beta factor represents the crustal thinning as a ratio of the crust thickness at a
 209 given time over the initial crust thickness as:

$$210 \quad \beta_n = \frac{hc_{t=n}}{hc_{t=0}} \quad (8)$$

211 Where β_n is the beta factor at time n , $hc_{t=n}$ is the crustal thickness at time n , and $hc_{t=0}$ is the initial
 212 crustal thickness.

213 Figure 11 represents the rift obliquity with respect to the extension direction. In order to compute the
 214 rift obliquity we define two boundaries depending on the beta factor value. The boundary labelled
 215 OCT (Ocean-Continent Transition) corresponds to the highest beta factor value (i.e. the location where
 216 the crust is the thinnest before the exhumed mantle) and the boundary labelled “necking” corresponds
 217 to the contour of the beta factor value equal to 2. Then we extract discrete points located on these
 218 contours and use the dot product between a vector defined by two points located on these contours
 219 (\vec{u}_c) and a vector defining the boundary condition velocity (\vec{v}_b) to compute the angle γ such as:

$$220 \quad \gamma = \cos^{-1} \left(\frac{\vec{u}_c \cdot \vec{v}_b}{\|\vec{u}_c\| \times \|\vec{v}_b\|} \right) \quad (9)$$

221 In order to highlight the first order structure orientation we then average the value of γ on rift segments
 222 of 20 km.



223 4. Numerical models results

224 In this study, we conducted ten experiments with a resolution of $\sim 2 \text{ km} \times 2 \text{ km} \times 2 \text{ km}$ per element.
225 Five simulations with a weak lower crust, and five simulations with a strong lower crust for angles of
226 extension $\alpha = 15^\circ, 30^\circ, 45^\circ, 60^\circ$ and 75° have been run. From these ten simulations setups three were
227 selected and run at higher resolution ($\sim 1 \text{ km} \times 1 \text{ km} \times 1 \text{ km}$ per element). The three selected
228 simulations are weak lower crust; $\alpha = 60^\circ$; and strong lower crust; $\alpha = 45^\circ$ and 15° . These three
229 models better capture the detailed structures associated with evolution of offset rift basins linked by
230 strike-slip structures and allow imaging very precisely the progressive formation and evolution of
231 strike-slip and transform margins. Therefore, we present in details the evolution through time and
232 space of these three models before summarising the results of all the lower resolution simulations.

233 4.1. Model 1: Weak lower crust, 60° extension

234 Deformation starts to localize around 5 Myr and isolated grabens individualise. These grabens are
235 limited by extensional to transtensional en-échélon faults oriented almost perpendicularly ($\sim \text{N}110$) to
236 the extension direction (Fig. 3a and 4A). From 15 Myr, as strain localizes more intensively in basins,
237 the en-échélon deformation re-organizes (Fig. 3g and 4C). Newly formed strike-slip faults in shear
238 zones oriented $\text{N}75$ link the $\text{N}110$ trending normal faults in the basins. The initial normal faults that
239 are no more active start to rotate clockwise along the diffuse strike-slip structures (Fig. 3h and 3k). A
240 differential thinning of the crust occurs between strike-slip fault zones and dip-slip deformation zones
241 leading to basins individualization (Fig. 3i). Then, strike-slip linkage occurs (Fig. 3j) to form large-
242 scale transfer zones ($\sim 100 \text{ km}$ long; $\sim 50 \text{ km}$ width) between offset basins. The major large-scale
243 transfer zone is localized along pre-existing damaged zone. Strike-slip shear zones display a $\text{N}60$
244 surface orientation and a dip of 90° (Fig. 4D and 4E, Cross section b-b') while newly formed
245 divergent shear zones show a $\sim \text{N}95$ surface orientation. Strike-slip and divergent shear zones form an
246 angle of 35° between each other and an angle of 30° and 65° with the extension direction. With the
247 strike-slip strain localization, small regions with transient compressional stress regimes appear in the
248 strike-slip to divergent transition zones accommodating the clockwise rotation (Fig. 3g and 3j). During
249 the rifting phase, normal faults formed at the early stages of thinning are passively rotating. As they
250 approach the strike-slip transfer zones their orientation change through time from $\text{N}110$ (at 5 Myr, Fig.
251 3a) to $\text{N}10$ (at 30 Myr, Fig. 3p) showing a clockwise rotation of $\sim 100^\circ$. Finally, when the mantle
252 exhumes and ridge accretion takes place (Fig. 3p), the continental lithosphere retrieves a rigid
253 behaviour and deformation only localizes in the mantle along transfer fault zones oriented $\text{N}80$ to
254 $\text{N}100$.

255 The final geometry of the continental margins is dominated by divergent segments that are parallel to
256 the exhumation age mantle stripes (i.e., to magnetic anomalies, Fig. 3q), while margin segments
257 located close to strike-slip faults zones are perpendicular to these mantle stripes (Fig. 3q). Offset
258 divergent basins are bounded by strike slip fault zones controlling ridge propagation. The orientation
259 of these segments highlights that the ridge propagation along strike stops until the strike-slip faults
260 zones start to accommodate mantle exhumation. As shown by the evolution of the rift through time,
261 under constant plate kinematics, the active deformation regime changes and re-orientes.

262 4.2. Model 2: Strong Lower Crust, 45° extension

263 In this model, the deformation starts to localize as extensional shear zones at the edges of the initial
264 damaged zones (Fig. 5a and 6A). Inside the weak zones, active deformation zones trend perpendicular
265 ($\sim \text{N}130$) to the extension direction while at the weak zones edges deformation is oriented $\text{N}110$. The
266 stress field evidences weak and diffuse compression that accommodates the shear zones orientation
267 variations between damaged zones (Fig. 5a). Areas situated between localized shear zones show a



268 diffuse strike-slip stress field. As thinning progresses, the deformation localizes more intensively in
269 the basins along shear zones oriented N110 (Fig. 5d and 6B). Between the basins, the active
270 deformation is localizing along N70 transfer zones with a sigmoid shape. The shear zones orientation
271 evolves from N90 at the edge of the basins to N70 (Fig. 5d) where elongated lower crustal domes
272 exhume in the transition zones between basins and strike-slip shear zones (Fig. 5e). The associated
273 stress field also display variations from purely strike-slip to transtensional (Fig. 5d). At 10 Myr, the
274 transfer zones show transtensional deformation in the most localized deformation area (Fig. 5d), while
275 at 15 Myr strike-slip deformation dominates (Fig. 5g). Once pure strike-slip deformation takes place in
276 the central part of the transfer zones (from 15 Myr), strain partitioning intensifies. The transfer zones
277 are divided in three domains, (1) the most external domain dominated by pure extension, (2) a
278 transitional domain dominated by transtensional deformation and (3) the central domain dominated by
279 pure strike-slip (Fig. 5g). These three domains are visible in cross-section (Fig. 6C, cross-section a-a'
280 and e-e') where two normal shear zones located on the borders of the transfer zones accommodate the
281 thinning of the lithosphere while in the centre a vertical shear zone accommodates the horizontal
282 displacement. From 18 Myr, ridge dynamics takes place in the basins (Fig. 5j and 6D). The transition
283 region between basins and transfer zones displays small en-échelon shear zones with compressional
284 stresses at their tips accommodating local clockwise rotation (Fig. 5j). At 30 Myr, the continental crust
285 in the transfer zones finally breaks up and the oceanic domain display a suite of interconnected basins
286 with sigmoid shapes (Fig. 5q).

287 The final structure of the continental margins (at 30 Myr) shows a spatial repetition of three segments
288 associated respectively with divergent, transtensional and strike-slip kinematics. The divergent
289 segments are parallel to the mantle exhumation age stripes and to the main necking faults located
290 along the initial weak zones (Fig. 5q). Transitional segments, located between the divergent and the
291 strike-slip segments show exhumed lower crustal and mantle domes (Fig. 5q and 6F). The deformation
292 pattern combines strike-slip, extensional and transitory compressional structures formed during the
293 evolution of the rift system. They are related to stress field dynamics with rotation between basins that
294 are mainly divergent and transfer zones that are mainly strike-slip. Finally, the strike-slip segments
295 form the third part of the margins where the mantle exhumed domain is the narrowest. The
296 deformation pattern is relatively simple with a strike-slip shear zone at the centre and only few
297 preserved normal faults in the thinned continental domain.

298 *4.3. Model 3: Strong Lower crust, 15° extension*

299 In this model, the deformation initiates as a wide and diffuse strike-slip region without clear individual
300 faults or shear zones, excepted along the model borders (Fig. 7a and 8A). At 10 Myr, the deformation
301 already localizes along a central vertical strike-slip shear zone oriented N90 and two surrounding
302 normal shear zones (Fig. 7d and 8B cross-section a-a'). From this stage, the deformation in the central
303 part of the model located between initial damaged weak zones evolves from strike-slip to
304 transtensional and extensional (Fig. 7g and 7j). Basins develop in these zones accommodate the
305 maximum vertical displacement (Fig. 7l). At the same time, between and around these basins, the
306 deformation progressively localizes as transtensional to vertical strike-slip shear zones oriented N70 to
307 N90 (Fig. 7j and 8D). Then at 25 Myr the deformation partitions between large scale (~500 km long)
308 strike-slip shear zones oriented N80 and extensional shear zones in between (Fig. 7m and 8E). The
309 strike-slip motion leads to the clockwise rotation of individualized blocks. This rotation produces
310 transient compressive strain in the hinges of the blocks (Fig. 7m and 7p). While during the first
311 deformation phase (from 0 Myr to 20 Myr) the extensional deformation localized along N90 shear
312 zones, during the second phase the extensional structures located between the large scale transform
313 faults display a N105 orientation (Fig. 7m and 7p). Compared to the two previous models, the crust



314 thins slower and at 30 Myr the mantle is not exhumed yet. In addition, the maximum crustal thinning
315 occurs between the initial damaged zones between the strike-slip shear zones. However, the cross-
316 section b-b' (Fig. 8B) following the orientation of the transform faults and crossing the normal faults
317 perpendicularly shows a hyper-thinned margin over ~300 km. The high obliquity of the extension
318 velocity favours horizontal displacements over vertical ones. This results in a relative dextral motion
319 of ~200 km on each transform shear zones in 30 Myr while continental break-up has not yet occurred.

320 The final structure of the continental margins (at 30 Myr) shows three strike-slip dominated shear zone
321 that are parallel to the extensional direction limiting two elongated extensional segments (Fig. 7p and
322 7q).

323 *4.4. Effect of obliquity and rheology on strain localization and rift evolution*

324 Figure 9 shows the results of all 2 km x 2 km x 2 km resolution simulations at 30 Myr. The models
325 results show that for the same extension direction, the rheology of the crust exerts a first order control
326 on the rift evolution and margin final structure. The 75° oblique extension models are drastically
327 different for a strong (Fig. 9q and 9r) and a weak lower crust (Fig. 9s and 9t). Although the small
328 degree of obliquity, a weak lower crust leaves more freedom in the model for stress rotation in the
329 crust and favours the development of individual offset basins which are linked by transfer fault zone.
330 This transfer fault zone results from the evolution of the en-échelon distributed deformation that
331 progressively localizes as described in the section 4.1 (Model 1). For a strong lower crust, the
332 deformation localizes faster on fewer shear zones and basins develop with a small offset. This strain
333 localization behaviour is different for a direction of extension of 45°. For these simulations, the model
334 with a strong lower crust (Fig. 9i and 9j) develops offset basins while for a weak lower crust (Fig. 9k
335 and 9l) basins are aligned. Finally, for high obliquity ($\alpha=15^\circ$) both strong (Fig. 9a and 9b) and weak
336 lower crust (Fig. 9c and 9d) models show that the strike-slip deformation drives the evolution of the
337 rift and results in large-scale transform shear zones.

338 These results tend to demonstrate that in order to form large scale strike-slip deformation that evolves
339 into strike-slip margin segments, the early formation of offset basins is essential in contexts of low to
340 intermediate obliquity. However, in context of important obliquity, the strike-slip deformation drives
341 the evolution of the system as soon as the deformation starts to localize.

342 The modelled rift evolution shows that the deformation of the continental lithosphere takes place in
343 three stages. The first stage corresponds to the initiation of the deformation in a rigid plate. For
344 obliquity angles larger than 30° the deformation always initiates along extensional shear zones
345 oriented sub-perpendicular to the extension direction. On the contrary, for obliquity angles below 30°
346 the deformation initiates along strike slip shear zones almost parallel to the imposed velocity field
347 vectors. This behaviour corresponds to the expected strain localization in a rigid plate. However, the
348 second stage of deformation marks significant change in strain regime and localization. The timing for
349 the initiation of this second stage may differ depending on the initial rheology of the lithosphere
350 (strong and weak crust) and the angle of extension but it is always observed. During this phase, the
351 stress field changes and the initial shear zones start to re-orient. For angles of obliquity greater than
352 30° the strike-slip deformation takes place along transfer fault zones to link the offset basins and
353 accommodate the oblique component of the velocity field. Rotation of former faulted blocks is the
354 result of this stress field reorientation at the corner between transfer fault zones and divergent
355 segments, where lower crust exhumation may occur. While for angles of obliquity lower than 30°, the
356 initial strike-slip deformation partitions to later form extensional shear zones that accommodate the
357 vertical displacement. Mechanically, the rheology of the lithosphere evolves from a rigid continuous
358 plate to a weakening domain in which the deformation localizes and temperature increases, which



359 contributes to the weakening of the lithosphere. This deformation stage is transient and evolves to the
360 third deformation stage which corresponds to the formation of a new plate boundary where the
361 deformation is highly localized and partitioned along a continuous shear zone separating again two
362 rigid plates.

363 *4.5. Lithosphere thickness evolution*

364 Figure 10 shows the evolution through time of the crustal thickness and thinning rate for each model.
365 Thickness evolution curves display the crustal thickness evolution in a selected zone located in a basin
366 (i.e. where the extension is maximal), in a strike-slip transfer zone, and in the transition zone between
367 the basin and the transfer zone. At first order, the thinning of the crust is faster in low obliquity models
368 than in high obliquity models (Fig. 10). Low to intermediate oblique extension models favour the
369 formation of extensional shear zones delimiting large basins between which strike-slip transfer zones
370 develop and therefore the vertical displacements are greater than the horizontal displacements.
371 Oppositely, high obliquity extension favours the formation of long strike-slip structures between
372 which small basins develop. In this context the horizontal motion is predominant over the vertical
373 motion and the thinning of the continental crust and lithosphere is 2 to 4 times slower than under low
374 and intermediate obliquity extension for the same plate velocity. The rheology of the crust also
375 controls the thinning rate since the deformation is more distributed in a weak crust than in a strong
376 crust, a longer time is necessary to achieve the same thinning of the crust.

377 For low to intermediate obliquity models (from $\alpha = 75^\circ$ to $\alpha = 45^\circ$) the thinning of the crust occurs in
378 different phases related to the deformation regime of the lithosphere. The first thinning phase is fast
379 (between 3 mm/yr and 4 mm/yr) and corresponds to the localization of extensional structures. Then,
380 during the second phase (stress re-orientation), while the strike-slip structures start to form, the
381 thinning of the crust slows down (between 1 mm/yr and 2 mm/yr). This slowing down is marked by a
382 peak in the thinning rate curves. A delay can also be observed between basins and strike-slip transfer
383 zones where achieving the same amount of thinning can take more time due to the decrease of the
384 vertical velocity component and the increase of the horizontal one in strike-slip shear zones.

385 **5. Comparison with previous modelling studies**

386 *5.1. Strain localization*

387 Modelling experiments involving oblique boundary conditions (Brune, 2014; Brune et al., 2012; this
388 study), offset weak zones (Allken et al., 2012; Le Pourhiet et al., 2017; Zwaan et al., 2016), or oblique
389 weak zones (Agostini et al., 2009; Ammann et al., 2017; Corti, 2012; Duclaux et al., 2020) show that
390 strain localization in the continental lithosphere always begins as extensional structures sub-
391 perpendicular to the extension direction for angles between extension direction and the weak zones
392 larger than $\sim 30^\circ$. Then, as the lithosphere thins and weakens due to mechanical and thermal softening,
393 deformation patterns evolve, and strain is partitioned between extensional and strike-slip segments.
394 Nevertheless, the orientation of these strike-slip segments is not parallel to the imposed plate motion
395 direction, but to local variations of the velocity field. Moreover, the orientation of the tectonic
396 structures changes through time although the global plate motion is kept constant (Brune, 2014;
397 Duclaux et al., 2020; Jourdon et al., 2020; Philippon et al., 2015; Le Pourhiet et al., 2017). For angles
398 of obliquity lower than $\sim 30^\circ$ the models with oblique boundary conditions show that strike-slip
399 deformation dominates (e.g. Brune, 2014) at the onset of intra-continental rifting. Then, localization
400 leads to strain partitioning between pure strike-slip shear zones and extensional shear zones
401 accommodating a small amount of vertical motion and promoting crustal thinning. However, in these
402 highly oblique cases, the vertical motion is very low and the continental lithosphere thins two times



403 slower than for the same velocity with lower obliquity (Fig. 10) (e.g. Brune et al., 2018). Among the
404 models involving cylindrical boundary conditions but offset or oblique weak zones, this degree of
405 obliquity is never reached due to the free-slip boundary condition. Except in presence of very efficient
406 mechanical softening processes (Ammann et al., 2017), two rifts develop and never link (e.g. Le
407 Pourhiet et al., 2017). Therefore, to study systems with very high obliquity, models need to take into
408 account limitations associated with the boundary conditions they use.

409 *5.2. Obliquity and offset structures*

410 Brune et al., (2012) and Brune et al., (2018) showed that oblique rifting requires less forces than
411 cylindrical rifting during the deformation of the continental lithosphere. However, transform and
412 strike-slip margins do not represent the majority of non-convergent margins (Mercier de Lépinay et
413 al., 2016). Models suggest that the formation of offset structures is essential to produce the association
414 of strike-slip or transform segments and divergent segments (e.g. Allken et al., 2012; Ammann et al.,
415 2017; Duclaux et al., 2020; Le Pourhiet et al., 2017; Zwaan et al., 2016). Although the formation of
416 offset structures is intrinsic in models involving offset or oblique weak zones and cylindrical boundary
417 conditions, with oblique boundary conditions the deformation does not necessarily develops offset
418 basins linked by strike-slip shear zones (Brune, 2014; Brune et al., 2012). Thermo-mechanical
419 numerical models involving oblique boundary conditions applied to a uniform lithosphere with one
420 straight weak zone (Brune, 2014; Brune et al., 2012) shows that the deformation localizes to
421 progressively form a unique straight shear zone and straight margins. Models conducted in this study
422 have the same oblique boundary conditions but present three separated weak zones rather than a
423 continuous one. These weak zones allow more freedom for structures to develop inside the model and
424 favour the localization of offset structures. For low to intermediate obliquity, they favour the
425 formation of offset basins while for high obliquity they favour the formation of offset strike-slip shear
426 zones. As shown on Figure 9, the offset between structures is essential to facilitate strain partitioning
427 and to form divergent and strike-slip segments. In models where basins form aligned to each other,
428 only one straight transtensional shear zone develops, while where basins (or strike-slip structures)
429 form with an offset, the deformation partitions between divergent and strike-slip segments (Fig. 11). A
430 first order implication of this result is that although oblique rifting may be ubiquitous (Brune et al.,
431 2018; Mélody Philippon & Corti, 2016) structural inheritance and previous geodynamic events should
432 play an important role in the initial localization pattern of offset structures and therefore transform
433 margins.

434 *5.3. Transform and strike-slip margins*

435 The kinematic conceptual model currently used to interpret and reconstruct the formation of transform
436 margins (e.g. Basile, 2015; Mascle & Blarez, 1987) has already been questioned by thermo-
437 mechanical models (e.g. Le Pourhiet et al. 2017). Indeed, our results show that during the intra-
438 continental oblique rifting phase, the lithosphere does not behave solely as a rigid plate but shear
439 structures are dynamic, and the deformation pattern changes as deformation progresses. The
440 continental lithosphere rheology evolves through time in favour of mechanical and thermal softening
441 (Fig. 12). Therefore, especially for obliquity angle greater than 30° , it is highly unlikely that transform
442 margins initiate from already segmented ridge-transform fault-ridge system, but rather emerge from
443 the progressive evolution of the stress field coupled with local heterogeneities in the lithosphere.
444 Moreover, although the definition that a transform fault is a strike-slip fault forming a plate boundary
445 parallel to the plate relative motion, analogue and numerical models suggest that except for high
446 obliquities, the strike-slip transfer zones formed during continental extension are not necessarily
447 parallel to the global plate motion (Fig. 11) but to the local velocity field, which contrast with oceanic
448 transform faults that form parallel to the plates motion (Gerya, 2012, 2013). On the one hand, for



449 intermediate to low obliquity cases (45° to 75°), the modelled margins that develop strain partitioning
450 display divergent segments oriented between 90° (orthogonal) and 60° , and strike-slip segments
451 oriented between 20° and 50° with respect to the imposed extension direction (Fig. 11e to 11g). These
452 margins present the first order characteristics of transform margins. Indeed, they display offset basins,
453 strike-slip and divergent segments and rotation of the tectonic structures in the (inner or outer corner)
454 concave and convex transition zones between the strike-slip and the divergent margins. On the other
455 hand, the high obliquity margins develop strike-slip faults parallel to the global relative plate motion.
456 The rift system is no more segmented in basins and transfer shear zones but displays pull-apart basins
457 oriented between 0° and 30° with respect to the extension direction (Fig. 11a to 11d). Highly oblique
458 systems, also present a very slow extension (Fig. 10), a rather cold lithosphere (1300°C isotherm at
459 120 km while the crust is only few kilometre thick) and small length – large width basins. Our
460 numerical models show that even a small amount of obliquity in extension direction can result in
461 important obliquity of the rift structures and trend (Fig. 11) and therefore corroborate that “oblique
462 rifting [is] the rule not the exception” (Brune et al., 2018).

463 6. Comparison with natural cases

464 Figure 1 shows natural examples of transform margins formed at different obliquities and presenting
465 very different structures. Indeed, the Gulf of California shows a rift system with small basins
466 segmented by large scale strike-slip faults and a dynamics very similar to high obliquity extension
467 models. In contrast, the Equatorial Atlantic displays large oceanic basins surrounded by continental
468 margins showing alternating strike-slip transfer zones linking long divergent segments (hundreds of
469 km). The African and South American margins share clearly more similarities with intermediate
470 oblique extension models than highly oblique ones.

471 6.1. Intermediate obliquity rift systems

472 The Equatorial Atlantic margins represent an historic natural case for which the conceptual and
473 kinematic models of transform margins has been established (Basile, 2015; Mascle & Blarez, 1987).
474 The Equatorial Atlantic is part of a larger scale rifting system leading to Gondwana fragmentation and
475 individual offset basins connected by transform faults during the Mesozoic. Continental margins
476 emerging from this major extensional event display individual offset basins connected by transform
477 faults such as the Mozambique-East Antarctica margins (e.g. Thompson et al., 2019), the Central
478 Atlantic margins (e.g. Schettino & Turco, 2009) and the Equatorial Atlantic margins (e.g. Heine et al.,
479 2013). Kinematic reconstructions of the Equatorial Atlantic opening succeed to reconstruct the oceanic
480 opening phase but present gaps, overlaps and misfits of major structures and cratonic bodies for the
481 intra-continental rifting phase. These errors mainly come from the non rigid behaviour of the
482 lithosphere and the locally varying velocity field that cannot be produced in kinematic models. Indeed,
483 our models show that during the intra-continental rifting phase, the stress field, and therefore the
484 structures associated, strongly varies along the rift. However, these variations are not due to plates’
485 kinematic changes, as the imposed velocity boundary condition is constant in our models, but to a
486 change in the rheological behaviour of the continental lithosphere. Indeed, while the continental
487 lithosphere behaves as a rigid plate when the deformation is localized along its plate boundaries, the
488 intra-plate strain localization process is characterized by the interactions between brittle and ductile
489 domains of the lithosphere. Moreover, the crustal and lithospheric thinning allows advecting warm
490 material from the exhuming mantle intensifying the non rigid behaviour of the lithosphere by
491 increasing the intensity of ductile deformation. Numerical models show that this is precisely during
492 this intra-continental rifting phase that strike-slip structures form and that rotation of early structures
493 occurs (Fig. 12e) (e.g. Duclaux et al., 2020).



494 In the Equatorial Atlantic rift system, two offset basins (the Central Atlantic basin to the Northwest
495 and the South Atlantic basin to the Southeast) connect in the future Central Atlantic basin forming an
496 East stepping system of dextral strike-slip fault zones (e.g. Heine et al., 2013).

497 Along the Romanche transform fault (Fig. 1b), the finite deformation shows pull-apart basins with
498 various faults orientations and isolated rotated blocks (e.g. Davison et al., 2016; Mascle & Blarez,
499 1987). Numerical models especially display structures rotation at the junction between divergent
500 segments and transfer strike-slip shear zones. The rotation of tilted blocks associated with a horsetail
501 splay is also observed at the junction between transform and divergent plate boundaries in analogue
502 experiments as well (e.g. Basile & Brun, 1999).

503 Finally, the continental deformation along the Romanche Transform fault zone is not a single highly
504 localized strike-slip fault but constitutes a deformation corridor of 40 km to 70 km wide in which
505 normal, reverse, strike-slip faults, or a combination of these are present (Basile et al., 1993; Nemčok et
506 al., 2012). This wide deformation zone in which a main strike-slip structure finally localizes well
507 illustrates the progressive strain localization process as shown in numerical models.

508 *6.2. High obliquity rift systems*

509 The Gulf of California represents the most compelling example of a highly oblique rift system. In
510 relation with the dextral San Andreas Fault system, the Gulf of California is an active plate boundary
511 formed in response to the relative motion between the Pacific and North America plates of ~5mm/a
512 (Plattner et al., 2007). Since ~12 Ma, the cessation of the Pacific plate's subduction beneath the Baja
513 California led to a major change in plate kinematics (Atwater & Stock, 1998; DeMets & Merkouriev,
514 2016; McKenzie & Morgan, 1969). This event is responsible of the highly oblique extension in the
515 Gulf of California (Lizarralde et al., 2007). The structural analysis performed on faults and shear zones
516 shows that the average angle between the rift system and the extension direction is ~20° (e.g. Bonini et
517 al., 2019). Moreover, the general trend of normal faults strike in the continental margin shows a NNW
518 orientation while the strike-slip faults display a NW-SE strike, indicating a ~20° difference in
519 orientation. Several models were proposed to interpret the surface deformation evolution through time
520 and space in the Gulf of California between ~12 Ma and present day. These models involve two end-
521 members, one implying a progressive change in the deformation regime firstly dominated by extension
522 (between 12 Ma and 6 Ma) and followed by dextral shear (from 6 Ma to present) (e.g. Darin et al.,
523 2016; Spencer & Normark, 1979; Stock & Hodges, 1989) and the other implying a coexistence of
524 strike-slip faults and normal faults since ~12 Ma (e.g. Fletcher et al., 2007; Seiler et al., 2010).

525
526 The numerical models presented in this study are not specifically designed for particular natural rifts,
527 especially in terms of imposed velocities or tectonic inheritances. However, the high obliquity
528 numerical model (extension angle $\alpha=15^\circ$) shows striking first order similarities with the Gulf of
529 California rift system and may bring new insights regarding the strain localization in highly oblique
530 rifts such as the Gulf of California. For constant boundary conditions (1 cm/a, 15° obliquity) the strain
531 localizes along normal shear zones forming a ~15° angle with the extension direction located at the
532 boundaries of the rift system while in its central part a large scale strike slip shear zone develops. The
533 deformation regime then evolves to transtension and forms pull-apart basins separated by strike-slip
534 shear zones parallel to the plate motion. The system then reaches a stable partitioned state with large
535 transform faults in the central part of the rift separating pull-apart basins and normal faults on the
536 edges parallel to the rift trend. Moreover, the high obliquity favours horizontal strike-slip motion over
537 vertical motion resulting in a dextral displacement of 200 km while break-up did not occurred yet. In
538 the Gulf of California the strike-slip motion since the Miocene (~12 Ma) represents 200 km to 300 km
539 (DeMets & Merkouriev, 2016; Stock & Hodges, 1989).



540

541 Therefore, the numerical model tends to show that the deformation could be partitioned since the onset
542 of highly oblique continental rifting, but with a first phase of predominant extension preserved in the
543 continental margin and predominant dextral shear in the nascent oceanic/exhumed mantle domain
544 (Fig. 12a) and a second phase of predominant dextral deformation with pull-apart basins in between
545 (Fig. 12b) followed by the rotation of extensional structures (Fig. 12c).

546 Conclusion

547 Numerical models presented in this study show that:

- 548 - The strike-slip faults responsible for transform margins formation do not form parallel to the
- 549 plate motion except for highly oblique extension ($\alpha > 30^\circ$)
- 550 - En-échelon deformation and offset basins are required to develop strike-slip linkage shear
- 551 zones evolving to transform margin
- 552 - Localized strike-slip shear zones form after normal faults once the lithosphere is already
- 553 thermally and mechanically weakened.
- 554 - The lithosphere weakening leads to stress and strain re-orientation under same kinematic
- 555 boundary conditions

556

557 Figures captions

558 Figure 1: a) Simplified structural map of the Gulf of California rift system (modified from Bonini et
559 al., 2019; Ferrari et al., 2018; Fletcher et al., 2007). Large white arrows display the plate motion
560 between the North American plate and the Pacific plate from Plattner et al., (2007). b) Simplified
561 structural map of the Equatorial Atlantic rift system at 110 Ma modified from Heine et al., (2013). FZ:
562 Fault Zone.

563 Figure 2: Numerical models setup. a) 3D spatial representation of the model domain with the 3
564 initially damaged zones. b) Schematic representation in map view of the velocity boundary conditions.
565 α is the angle between the velocity vectors and the x direction. c) Yield stress envelopes and initial
566 geotherm of strong and weak lower crust models.

567 Figure 3: Model 1, Weak lower crust, $\alpha = 60^\circ$, map views. Left column: Active strain regime, the
568 intensity of the colours depends on the intensity of the second invariant of the strain rate. The
569 background represents the topography with hill shading. Central column: Plastic strain computed from
570 equation (A5) in the crust and exhumation ages of the mantle below 800°C isotherm. Right column:
571 Beta factor of the crust computed with equation (8).

572 Figure 4: Model 1, Weak lower crust, $\alpha = 60^\circ$. Map views and cross-sections of simulated lithologies
573 and second invariant of the strain rate tensor (equation 7).

574 Figure 5: Model 2, Strong lower crust, $\alpha = 45^\circ$, map views. Left column: Active strain regime, the
575 intensity of the colours depends on the intensity of the second invariant of the strain rate. The
576 background represents the topography with hill shading. Central column: Plastic strain computed from
577 equation (A5) in the crust and exhumation ages of the mantle below 800°C isotherm. Right column:
578 Beta factor of the crust computed with equation (8).



579 Figure 6: Model 2, Strong lower crust, $\alpha = 45^\circ$. Map views and cross-sections of simulated lithologies
580 and second invariant of the strain rate tensor (equation 7).

581 Figure 7: Model 3, Strong lower crust, $\alpha = 15^\circ$, map views. Left column: Active strain regime, the
582 intensity of the colours depends on the intensity of the second invariant of the strain rate. The
583 background represents the topography with hill shading. Central column: Plastic strain computed from
584 equation (A5) in the crust and exhumation ages of the mantle below 800°C isotherm. Right column:
585 Beta factor of the crust computed with equation (8).

586 Figure 8: Model 3, Strong lower crust, $\alpha = 15^\circ$. Map views and cross-sections of simulated lithologies
587 and second invariant of the strain rate tensor (equation 7).

588 Figure 9: Map view of the $2\text{ km} \times 2\text{ km} \times 2\text{ km}$ resolution models at 30 Myrs. The two left columns
589 display the strong lower crust models while the two right columns display the weak lower crust
590 models. For each model the second invariant of the strain rate tensor and the plastic strain and mantle
591 exhumation age are displayed.

592 Figure 10: Curves of crustal thickness in a), g) basins, b), h) transition zones, c), i) transfer/strike-slip
593 zones for strong and weak lower crust models. Curves of crustal thinning rate computed as the time
594 derivative of crustal thickness for d), j) basins, e), k) transition zones and f), l) transfer/strike-slip
595 zones for strong and weak lower crust models.

596 Figure 11: Map view of each model representing the angle of the Ocean-Continent Transition (OCT)
597 and the necking zone with respect to the extension direction.

598 Figure 12: Schematic simplified evolution of intracontinental deformation leading to the formation of
599 strike-slip and transform margins for high and intermediate obliquity based on numerical models
600 results.

601

602



603 **Appendix A**

604 To model the deformation of the lithosphere at geological timescales we use pTatin3D (May et al.,
605 2014, 2015). The code uses an Arbitrary Lagrangian-Eulerian (ALE) discretization with the material
606 point method to solve the conservation of momentum:

$$607 \quad \nabla \cdot (2\eta\dot{\boldsymbol{\epsilon}}) - \nabla P = \rho\vec{g} \quad (\text{A1})$$

608 where η is the non-linear effective viscosity, $\dot{\boldsymbol{\epsilon}}$ the strain rate tensor, P the pressure, ρ the density, \vec{g} the
609 gravity acceleration vector. The conservation of mass is solved for an incompressible fluid:

$$610 \quad \nabla \cdot \vec{v} = 0 \quad (\text{A2})$$

611 with \vec{v} as the velocity vector.

612 To consider the interactions between deformation and temperature, the Stokes flow is coupled with the
613 time dependent advection-diffusion energy conservation law:

$$614 \quad \frac{\partial T}{\partial t} + \vec{v} \cdot \nabla T = \nabla \cdot (\kappa \nabla T) + \frac{H}{\rho C_p} \quad (\text{A3})$$

615 where T is the temperature, \vec{v} the velocity vector of the fluid, κ the thermal diffusivity and C_p is the
616 heat capacity. The heat source H is the sum of the radiogenic heat production (eq. 2, in the main text)
617 and the shear heating heat production H_s :

$$618 \quad H_s = \frac{2\eta\dot{\boldsymbol{\epsilon}}^{\text{II}^2}}{\rho C_p} \quad (\text{A4})$$

619 According to the Boussinesq approximation the material density may vary with pressure and
620 temperature as:

$$621 \quad \rho = \rho_0(1 - \alpha(T - T_0) + \beta(P - P_0)) \quad (\text{A5})$$

622 where ρ_0 is the initial material density, α the thermal expansion coefficient and β the compressibility.

623 To solve the Stokes flow we use Q2-P1 elements while the energy conservation is solved with
624 a Q1 discretization. The top boundary of the domain is defined with a free surface boundary condition
625 evolving dynamically with the deformation.

626 *Rheological model*

627 The mechanical behaviour of the lithosphere at geological timescales is simulated with a visco-
628 plastic rheology. The brittle parts of the lithosphere are simulated with the Drucker-Prager pseudo-
629 plastic yield criterion adapted to continuum mechanics:

$$630 \quad \eta_p = \frac{C \cos(\phi) + P \sin(\phi)}{\dot{\boldsymbol{\epsilon}}^{\text{II}}} \quad (\text{A6})$$

631 where C is the cohesion (20 MPa), ϕ the friction coefficient, P the pressure and $\dot{\boldsymbol{\epsilon}}^{\text{II}}$ the second invariant
632 of the strain rate tensor. To simulate the mechanical softening in brittle faults, we apply a simple linear
633 decrease of the friction angle from 30° to 5° with accumulated plastic strain from 0 to 1 (equation 3 in
634 main text). Moreover, laboratory experiments show that under high confining pressures (> 1GPa)
635 rocks no more behave as brittle but as plastic materials (e.g. Kameyama et al., 1999; Precigout et al.,
636 2007). To consider that change we limit the Drucker-Prager yield stress to a maximum deviatoric
637 stress of 400 MPa according to the findings in Watremez et al. (2013).



638 The ductile deformation is modelled with the Arrhenius flow law for dislocation creep:

$$639 \quad \eta_v = A^{-\frac{1}{n}} (\dot{\epsilon}''')^{\frac{1}{n-1}} \exp\left(\frac{Q+PV}{nRT}\right) \quad (A7)$$

640 where A, n and Q are material dependant parameters (see Table 1), R is the gas constant and V is the
641 activation volume.

642 **Code availability**

643 Models of this study were produced with pTatin (May et al., 2014, 2015), an open source code for
644 geodynamics modelling publicly available at: <https://bitbucket.org/ptatin/ptatin3d/src/master/>.

645 **Authors contribution**

646 Anthony Jourdon designed, ran and post-processed the models, wrote the manuscript and produced the
647 figures. Charlie Kergaravat and Guillaume Duclaux contributed to results discussion and
648 interpretation, figures production and writing of the manuscript. Caroline Huguen contributed to the
649 conceptualization of the study.

650 **Competing interests**

651 Three of the authors were or are employed by the energy company TOTAL S.A. Models computing
652 was done on TOTAL's Pangea supercomputer.

653 **References**

654

- 655 Agostini, A., Corti, G., Zeoli, A., & Mulugeta, G. (2009). Evolution, pattern, and partitioning of
656 deformation during oblique continental rifting: Inferences from lithospheric-scale centrifuge
657 models. *Geochemistry, Geophysics, Geosystems*, 10(11). <https://doi.org/10.1029/2009GC002676>
- 658 Allken, V., Huisman, R. S., & Thieulot, C. (2012). Factors controlling the mode of rift interaction in
659 brittle-ductile coupled systems: A 3D numerical study. *Geochemistry, Geophysics, Geosystems*,
660 13(5), 1–18. <https://doi.org/10.1029/2012GC004077>
- 661 Ammann, N., Liao, J., Gerya, T., & Ball, P. (2017). Oblique continental rifting and long transform
662 fault formation based on 3D thermomechanical numerical modeling. *Tectonophysics*, (February),
663 1–16. <https://doi.org/10.1016/j.tecto.2017.08.015>
- 664 Atwater, T., & Stock, J. (1998). Pacific North America plate tectonics of the Neogene southwestern
665 United States: an update. *International Geology Review*, 40(5), 375–402.
666 <https://doi.org/10.1080/00206819809465216>
- 667 Basile, C. (2015). Tectonophysics Transform continental margins — part 1 : Concepts and models.
668 *Tectonophysics*, 661, 1–10. <https://doi.org/10.1016/j.tecto.2015.08.034>
- 669 Basile, C., & Brun, J. P. (1999). Transtensional faulting patterns ranging from pull-apart basins to
670 transform continental margins: An experimental investigation. *Journal of Structural Geology*,



- 671 21(1), 23–37. [https://doi.org/10.1016/S0191-8141\(98\)00094-7](https://doi.org/10.1016/S0191-8141(98)00094-7)
- 672 Basile, C., Mascle, J., Popoff, M., Bouillin, J. P., & Mascle, G. (1993). The Ivory Coast-Ghana
673 transform margin : a marginal ridge structure deduced from seismic data. *Tectonophysics*, 222,
674 1–19.
- 675 Basile, C., Maillard, A., Patriat, M., Gaullier, V., Loncke, L., Roest, W., ... Pattier, F. (2013).
676 Structure and evolution of the demerara plateau, offshore french guiana: Rifting, tectonic
677 inversion and post-rift tilting at transform-divergent margins intersection. *Tectonophysics*, 591,
678 16–29. <https://doi.org/10.1016/j.tecto.2012.01.010>
- 679 Bellahsen, N., Leroy, S., Autin, J., Razin, P., d'Acremont, E., Sloan, H., ... Khanbari, K. (2013). Pre-
680 existing oblique transfer zones and transfer/transform relationships in continental margins: New
681 insights from the southeastern Gulf of Aden, Socotra Island, Yemen. *Tectonophysics*, 607, 32–
682 50. <https://doi.org/10.1016/j.tecto.2013.07.036>
- 683 Bonini, M., Cerca, M., Moratti, G., López-Martínez, M., Corti, G., & Gracia-Marroquín, D. (2019).
684 Strain partitioning in highly oblique rift settings: Inferences from the southwestern margin of the
685 Gulf of California (Baja California Sur, México). *Tectonics*, 38(12), 4426–4453.
686 <https://doi.org/10.1029/2019TC005566>
- 687 Brune, S. (2014). Evolution of stress and fault patterns in oblique rift systems: 3-D numerical
688 lithospheric-scale experiments from rift to breakup. *Geochemistry, Geophysics, Geosystems*, 15,
689 3392–3415. <https://doi.org/10.1002/2014GC005446>.Received
- 690 Brune, S., & Autin, J. (2013). The rift to break-up evolution of the Gulf of Aden: Insights from 3D
691 numerical lithospheric-scale modelling. *Tectonophysics*, 607, 65–79.
692 <https://doi.org/10.1016/j.tecto.2013.06.029>
- 693 Brune, S., Williams, S. E., & Dietmar Müller, R. (2018). Oblique rifting: The rule, not the exception.
694 *Solid Earth*, 9(5), 1187–1206. <https://doi.org/10.5194/se-9-1187-2018>
- 695 Brune, S., Corti, G., & Ranalli, G. (2017). Controls of inherited lithospheric heterogeneity on rift
696 linkage: Numerical and analog models of interaction between the Kenyan and Ethiopian rifts
697 across the Turkana depression. *Tectonics*, 36(9), 1767–1786.
698 <https://doi.org/10.1002/2017TC004739>
- 699 Brune, S., Popov, A. A., & Sobolev, S. V. (2012). Modeling suggests that oblique extension facilitates
700 rifting and continental break-up. *Journal of Geophysical Research*, 117(B08402), 1–16.
701 <https://doi.org/10.1029/2011JB008860>
- 702 Buchmann, T. J., & Connolly, P. T. (2007). Contemporary kinematics of the Upper Rhine Graben: A
703 3D finite element approach. *Global and Planetary Change*, 58(1–4), 287–309.
704 <https://doi.org/10.1016/j.gloplacha.2007.02.012>
- 705 Le Calvez, J., & Vendeville, B. (2002). Experimental designs to model along-strike fault interaction
706 fault interaction. *Journal of the Virtual Explorer*, 7, 1–17.
707 <https://doi.org/10.3809/jvirtex.2002.00043>
- 708 Corti, G. (2012). Tectonophysics Evolution and characteristics of continental rifting : Analog



- 709 modeling-inspired view and comparison with examples from the East African Rift System.
710 *Tectonophysics*, 522–523, 1–33. <https://doi.org/10.1016/j.tecto.2011.06.010>
- 711 Darin, M. H., Bennett, S. E. K., Dorsey, R. J., Oskin, M. E., & Iriondo, A. (2016). Late Miocene
712 extension in coastal Sonora, México: Implications for the evolution of dextral shear in the proto-
713 Gulf of California oblique rift. *Tectonophysics*, 693, 378–408.
714 <https://doi.org/10.1016/j.tecto.2016.04.038>
- 715 Davison, I., Faull, T., Greenhalgh, J., Beirne, E. O., & Steel, I. (2016). Transpressional structures and
716 hydrocarbon potential along the Romanche Fracture Zone: a review. *Geological Society, London,*
717 *Special Publications*, 431, 235–248. <https://doi.org/10.1144/SP431.2>
- 718 Delvaux, D., Moeys, R., Stapel, G., Petit, C., Levi, K., Miroshnichenko, A., ... San'kov, V. (1997).
719 Paleostress reconstructions and geo-dynamics of the Baikal region, Central Asia, Part 2.
720 Cenozoic rifting. *Tectonophysics*, 282, 1–38. [https://doi.org/10.1016/S0040-1951\(97\)00210-2](https://doi.org/10.1016/S0040-1951(97)00210-2)
- 721 DeMets, C., & Merkouriev, S. (2016). High-resolution reconstructions of Pacific-North America plate
722 motion: 20 Ma to present. *Geophysical Journal International*, 207(2), 741–773.
723 <https://doi.org/10.1093/gji/ggw305>
- 724 Duclaux, G., Huisman, R. S., & May, D. A. (2020). Rotation, narrowing, and preferential
725 reactivation of brittle structures during oblique rifting. *Earth and Planetary Science Letters*, 531.
726 <https://doi.org/10.1016/j.epsl.2019.115952>
- 727 Ferrari, L., Orozco-Esquivel, T., Bryan, S. E., López-Martínez, M., & Silva-Fragoso, A. (2018).
728 Cenozoic magmatism and extension in western Mexico: Linking the Sierra Madre Occidental
729 silicic large igneous province and the Comondú Group with the Gulf of California rift. *Earth-*
730 *Science Reviews*, 183(June 2016), 115–152. <https://doi.org/10.1016/j.earscirev.2017.04.006>
- 731 Fletcher, J. M., Grove, M., Kimbrough, D., Lovera, O., & Gehrels, G. E. (2007). Ridge-trench
732 interactions and the Neogene tectonic evolution of the Magdalena shelf and southern Gulf of
733 California: Insights from detrital zircon U-Pb ages from the Magdalena fan and adjacent areas.
734 *Bulletin of the Geological Society of America*, 119(11–12), 1313–1336.
735 <https://doi.org/10.1130/B26067.1>
- 736 Gerya, T. (2012). Origin and models of oceanic transform faults. *Tectonophysics*, 522–523, 34–54.
737 <https://doi.org/10.1016/j.tecto.2011.07.006>
- 738 Gerya, T., & Burov, E. (2018). Nucleation and evolution of ridge-ridge-ridge triple junctions :
739 Thermomechanical model and geometrical theory. *Tectonophysics*, 746, 83–105.
740 <https://doi.org/10.1016/j.tecto.2017.10.020>
- 741 Gerya, T. V. (2013). Three-dimensional thermomechanical modeling of oceanic spreading initiation
742 and evolution. *Physics of the Earth and Planetary Interiors*, 214, 35–52.
743 <https://doi.org/10.1016/j.pepi.2012.10.007>
- 744 Heine, C., Zoethout, J., & Müller, R. D. (2013). Kinematics of the South Atlantic rift. *Solid Earth*,
745 4(2), 215–253. <https://doi.org/10.5194/se-4-215-2013>
- 746 Hergert, T., & Heidbach, O. (2011). Geomechanical model of the Marmara Sea region—II. 3-D



- 747 contemporary background stress field. *Geophysical Journal International*, 185, 1090–1102.
748 <https://doi.org/10.1111/j.1365-246X.2011.04992.x>
- 749 Hirth, G., & Kohlstedt, D. L. (2003). Rheology of the Upper Mantle and the Mantle Wedge: A View
750 from the Experimentalists. *Geophysical Monograph*, 138, 83–105.
- 751 Jourdon, A., Le Pourhiet, L., Mouthereau, F., & Masini, E. (2019). Role of rift maturity on the
752 architecture and shortening distribution in mountain belts. *Earth and Planetary Science Letters*,
753 512, 89–99. <https://doi.org/10.1016/j.epsl.2019.01.057>
- 754 Jourdon, A., Le Pourhiet, L., Mouthereau, F., & May, D. (2020). Modes of Propagation of Continental
755 Breakup and Associated Oblique Rift Structures. *Journal of Geophysical Research: Solid Earth*,
756 125(9), 1–27. <https://doi.org/10.1029/2020JB019906>
- 757 Kameyama, M., Yuen, D. A., & Karato, S. (1999). Thermal-mechanical effects of low-temperature
758 plasticity (the Peierls mechanism) on the deformation of a viscoelastic shear zone. *Earth and
759 Planetary Science Letters*, 168, 159–172.
- 760 Liao, J., & Gerya, T. (2015). From continental rifting to sea floor spreading : Insight from 3D thermo-
761 mechanical modeling. *Gondwana Research*, 28(4), 1329–1343.
762 <https://doi.org/10.1016/j.gr.2014.11.004>
- 763 Lizarralde, D., Axen, G. J., Brown, H. E., Fletcher, J. M., González-Fernández, A., Harding, A. J., ...
764 Umhoefer, P. J. (2007). Variation in styles of rifting in the Gulf of California. *Nature*, 448(7152),
765 466–469. <https://doi.org/10.1038/nature06035>
- 766 Lorenzo, J. M., & Vera, E. E. (1992). Thermal uplift and erosion across the continent-ocean transform
767 boundary of the southern Exmouth Plateau. *Earth and Planetary Science Letters*, 108(1), 79–92.
768 [https://doi.org/https://doi.org/10.1016/0012-821X\(92\)90061-Y](https://doi.org/https://doi.org/10.1016/0012-821X(92)90061-Y)
- 769 Mart, Y., & Dauteuil, O. (2000). Analogue experiments of propagation of oblique rifts.
770 *Tectonophysics*, 316, 121–132.
- 771 Mascle, J., & Blarez, E. (1987). Evidence for transform margin evolution from the Ivory Coast–Ghana
772 continental margin. *Nature*, 326(6111), 378–381.
- 773 May, D. A., Brown, J., & Le Pourhiet, L. (2014). pTatin3D : High-Performance Methods for Long-
774 Term Lithospheric Dynamics. *Proceeding SC'14 Proceedings of the International Conference
775 for High Performance Computing, Networking, Storage and Analysis*., 274–284.
- 776 May, D. A., Brown, J., & Le Pourhiet, L. (2015). A scalable , matrix-free multigrid preconditioner for
777 finite element discretizations of heterogeneous Stokes flow. *Computer Methods in Applied
778 Mechanics and Engineering*, 290, 496–523. <https://doi.org/10.1016/j.cma.2015.03.014>
- 779 McKenzie, D., & Morgan, W. J. (1969). Evolution of Triple Junctions. *Nature*, 224, 125–133.
780 <https://doi.org/10.1038/224125a0>
- 781 Mercier de Lépinay, M., Loncke, L., Basile, C., Roest, W. R., Patriat, M., Maillard, A., & De Clarens,
782 P. (2016). Transform continental margins – Part 2 : A worldwide review. *Tectonophysics*, 693,
783 96–115. <https://doi.org/10.1016/j.tecto.2016.05.038>



- 784 Milani, E. J., & Davison, I. (1988). Basement control and transfer tectonics in the Recôncavo-Tucano-
785 Jatobá rift, Northeast Brazil. *Tectonophysics*, *154*(1–2). <https://doi.org/10.1016/0040->
786 1951(88)90227-2
- 787 Mondy, L. S., Rey, P. F., Duclaux, G., & Moresi, L. (2018). The role of asthenospheric flow during
788 rift propagation and breakup. *Geology*, *46*(2), 103–106.
- 789 Nemčok, M., Sinha, S. T., Stuart, C. J., Welker, C., Choudhuri, M., Sharma, S. P., ... Venkatraman, S.
790 (2012). East Indian margin evolution and crustal architecture: integration of deep reflection
791 seismic interpretation and gravity modelling. *Geological Society, London, Special Publications*,
792 *369*, 477–496. <https://doi.org/10.1144/SP369.6>
- 793 Parsiegla, N., Stankiewicz, J., Gohl, K., Ryberg, T., & Uenzelmann-Neben, G. (2009). Southern
794 African continental margin: Dynamic processes of a transform margin. *Geochemistry*,
795 *Geophysics, Geosystems*, *10*(3). <https://doi.org/10.1029/2008GC002196>
- 796 Philippon, M., Willingshofer, E., Sokoutis, D., Corti, G., Sani, F., Bonini, M., & Cloetingh, S. (2015).
797 Slip re-orientation in oblique rifts. *Geology*, *43*(2), 147–150. <https://doi.org/10.1130/G36208.1>
- 798 Philippon, Mélody, & Corti, G. (2016). Obliquity along plate boundaries. *Tectonophysics*, *693*, 171–
799 182. <https://doi.org/10.1016/j.tecto.2016.05.033>
- 800 Plattner, C., Malservisi, R., Dixon, T. H., Lafemina, P., Sella, G. F., Fletcher, J., & Suarez-Vidal, F.
801 (2007). New constraints on relative motion between the Pacific Plate and Baja California
802 microplate (Mexico) from GPS measurements. *Geophysical Journal International*, *170*(3), 1373–
803 1380. <https://doi.org/10.1111/j.1365-246X.2007.03494.x>
- 804 Le Pourhiet, L., May, D. A., Huille, L., Watremez, L., & Leroy, S. (2017). A genetic link between
805 transform and hyper-extended margins. *Earth and Planetary Science Letters*, *465*, 184–192.
806 <https://doi.org/10.1016/j.epsl.2017.02.043>
- 807 Le Pourhiet, L., Chamot-Rooke, N., Delescluse, M., May, D. A., Watremez, L., & Pubellier, M.
808 (2018). Continental break-up of the South China Sea stalled by far-field compression. *Nature*
809 *Geoscience*. <https://doi.org/10.1038/s41561-018-0178-5>
- 810 Precigout, J., Gueydan, F., Gapais, D., Garrido, C. J., & Essaifi, A. (2007). Strain localisation in the
811 subcontinental mantle — a ductile alternative to the brittle mantle. *Tectonophysics*, *445*, 318–
812 336. <https://doi.org/10.1016/j.tecto.2007.09.002>
- 813 Ranalli, G., & Murphy, D. C. (1987). Rheological stratification of the lithosphere. *Tectonophysics*,
814 *132*, 281–295.
- 815 Rybacki, E., & Dresen, G. (2000). Dislocation and diffusion creep of synthetic anorthite aggregates.
816 *Journal of Geophysical Research: Solid Earth*, *105*(B11), 26017–26036.
817 <https://doi.org/10.1029/2000JB900223>
- 818 Schettino, A., & Turco, E. (2009). Breakup of Pangaea and plate kinematics of the central Atlantic and
819 Atlas regions. *Geophysical Journal International*, *178*(2), 1078–1097.
820 <https://doi.org/10.1111/j.1365-246X.2009.04186.x>



- 821 Scrutton, R. A. (1979). On Sheared Passive Continental Margins. *Developments in Geotectonics*, 15,
822 293–305. <https://doi.org/10.1016/B978-0-444-41851-7.50020-0>
- 823 Seiler, C., Fletcher, J. M., Quigley, M. C., Gleadow, A. J. W., & Kohn, B. P. (2010). Neogene
824 structural evolution of the Sierra San Felipe, Baja California: Evidence for proto-gulf
825 transtension in the Gulf Extensional Province? *Tectonophysics*, 488(1–4), 87–109.
826 <https://doi.org/10.1016/j.tecto.2009.09.026>
- 827 Simpson, R. W. (1997). Quantifying Anderson’s fault types. *Journal of Geophysical Research*,
828 102(17), 909–919. <https://doi.org/199710.1029/97JB01274>
- 829 Spencer, J. E., & Normark, W. R. (1979). Tosco-Abrejos fault zone: A Neogene transform plate
830 boundary within the Pacific margin of southern Baja California, Mexico. *Geology*, 7(11), 554–
831 557. [https://doi.org/10.1130/0091-7613\(1979\)7<554:TFZANT>2.0.CO;2](https://doi.org/10.1130/0091-7613(1979)7<554:TFZANT>2.0.CO;2)
- 832 Stock, J. M., & Hodges, V. K. (1989). Pre-Pliocene extension around the Gulf of California and the
833 transfer of Baja California to the Pacific plate. *Tectonics*, 8(1), 99–115.
- 834 Suckro, S. K., Gohl, K., Funck, T., Heyde, I., Schreckenberger, B., Gerlings, J., & Damm, V. (2013).
835 The davis strait crust-a transform margin between two oceanic basins. *Geophysical Journal
836 International*, 193(1), 78–97. <https://doi.org/10.1093/gji/ggs126>
- 837 Taylor, B., Goodliffe, A., & Martinez, F. (2009). Initiation of transform faults at rifted continental
838 margins. *Comptes Rendus Geoscience*, 341(5), 428–438.
839 <https://doi.org/10.1016/j.crte.2008.08.010>
- 840 Thompson, J. O., Moulin, M., Aslanian, D., de Clarens, P., & Guillocheau, F. (2019). New starting
841 point for the Indian Ocean: Second phase of breakup for Gondwana. *Earth-Science Reviews*, 191,
842 26–56. <https://doi.org/https://doi.org/10.1016/j.earscirev.2019.01.018>
- 843 Tron, V., & Brun, J. P. (1991). Experiments on oblique rifting in brittle-ductile systems.
844 *Tectonophysics*, 188(1–2), 71–84. [https://doi.org/10.1016/0040-1951\(91\)90315-J](https://doi.org/10.1016/0040-1951(91)90315-J)
- 845 Turcotte, D. L., & Schubert, G. (2002). *Geodynamics*. Cambridge University Press, Cambridge,
846 *Second Edition*. <https://doi.org/10.1007/s007690000247>
- 847 Watremez, L., Burov, E., D’Acremont, E., Leroy, S., Huet, B., Le Pourhiet, L., & Bellahsen, N.
848 (2013). Buoyancy and localizing properties of continental mantle lithosphere: Insights from
849 thermomechanical models of the eastern Gulf of Aden. *Geochemistry, Geophysics, Geosystems*,
850 14(8), 2800–2817. <https://doi.org/10.1002/ggge.20179>
- 851 Zwaan, F., Schreurs, G., Naliboff, J., & Buiter, S. J. H. (2016). Insights into the effects of oblique
852 extension on continental rift interaction from 3D analogue and numerical models.
853 *Tectonophysics*, 693, 239–260. <https://doi.org/10.1016/j.tecto.2016.02.036>
- 854
- 855



(Figure 1)

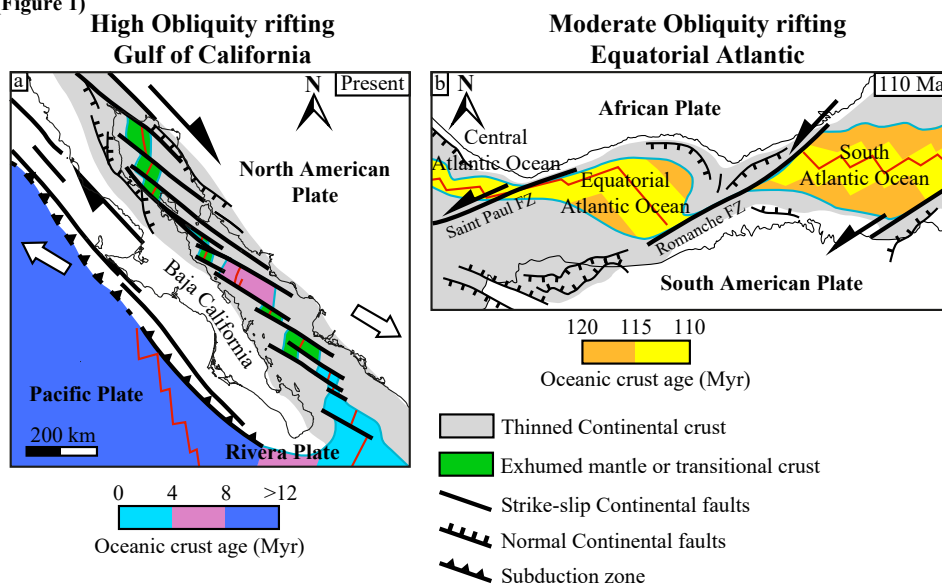




(Figure 2)

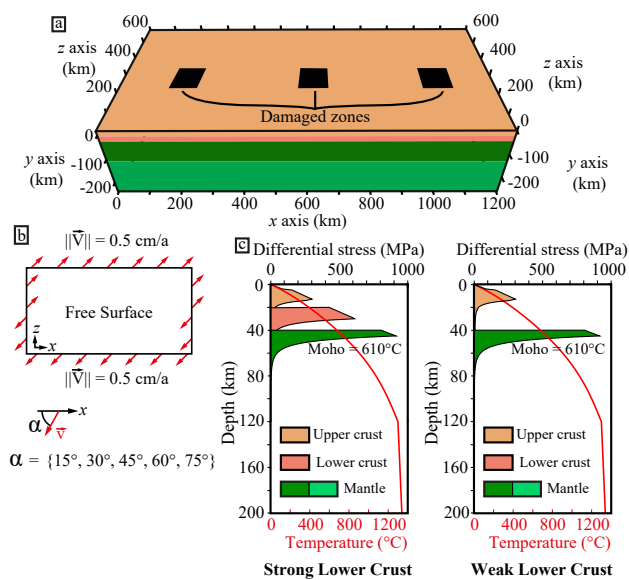




(Figure 3)

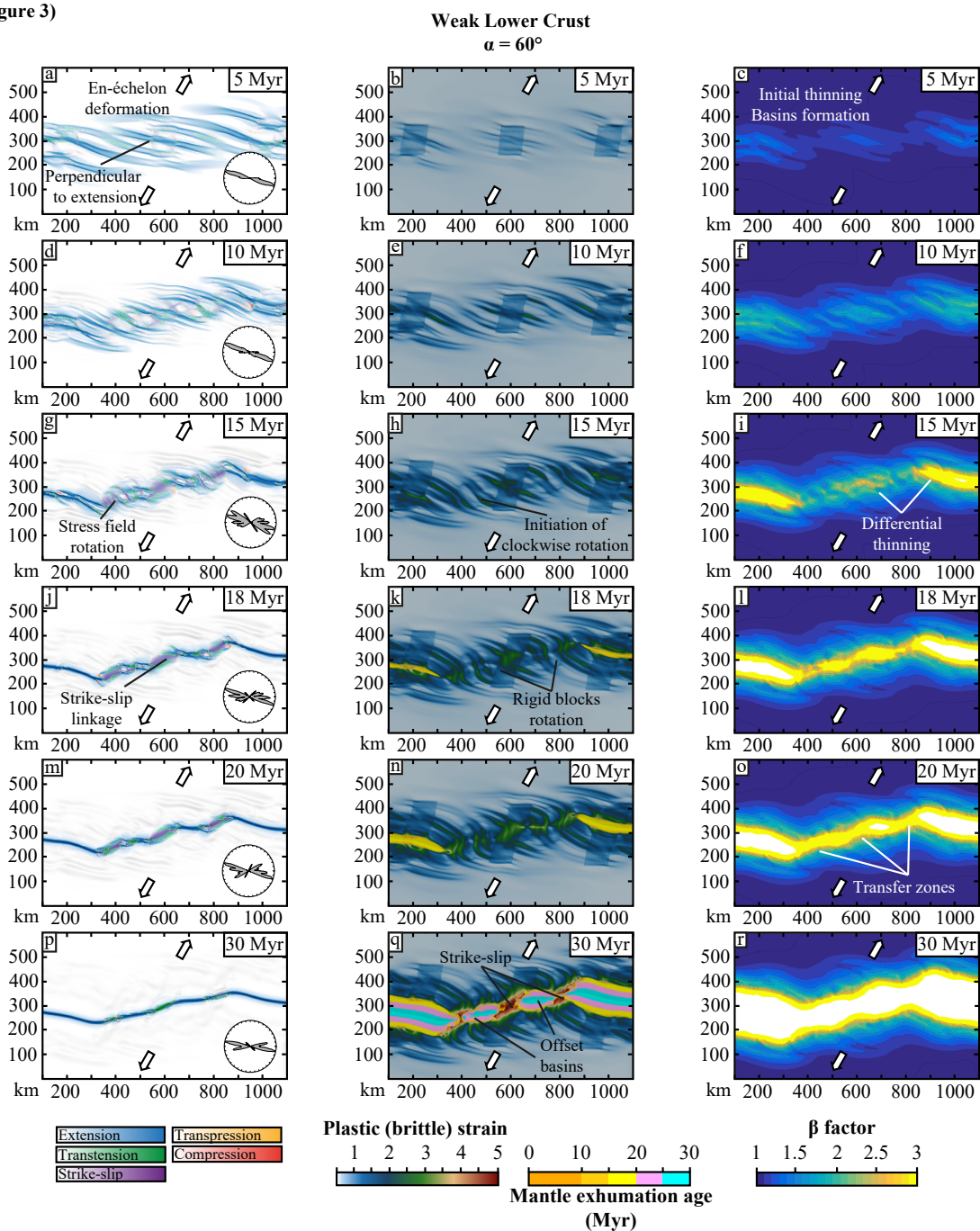




(Figure 4)

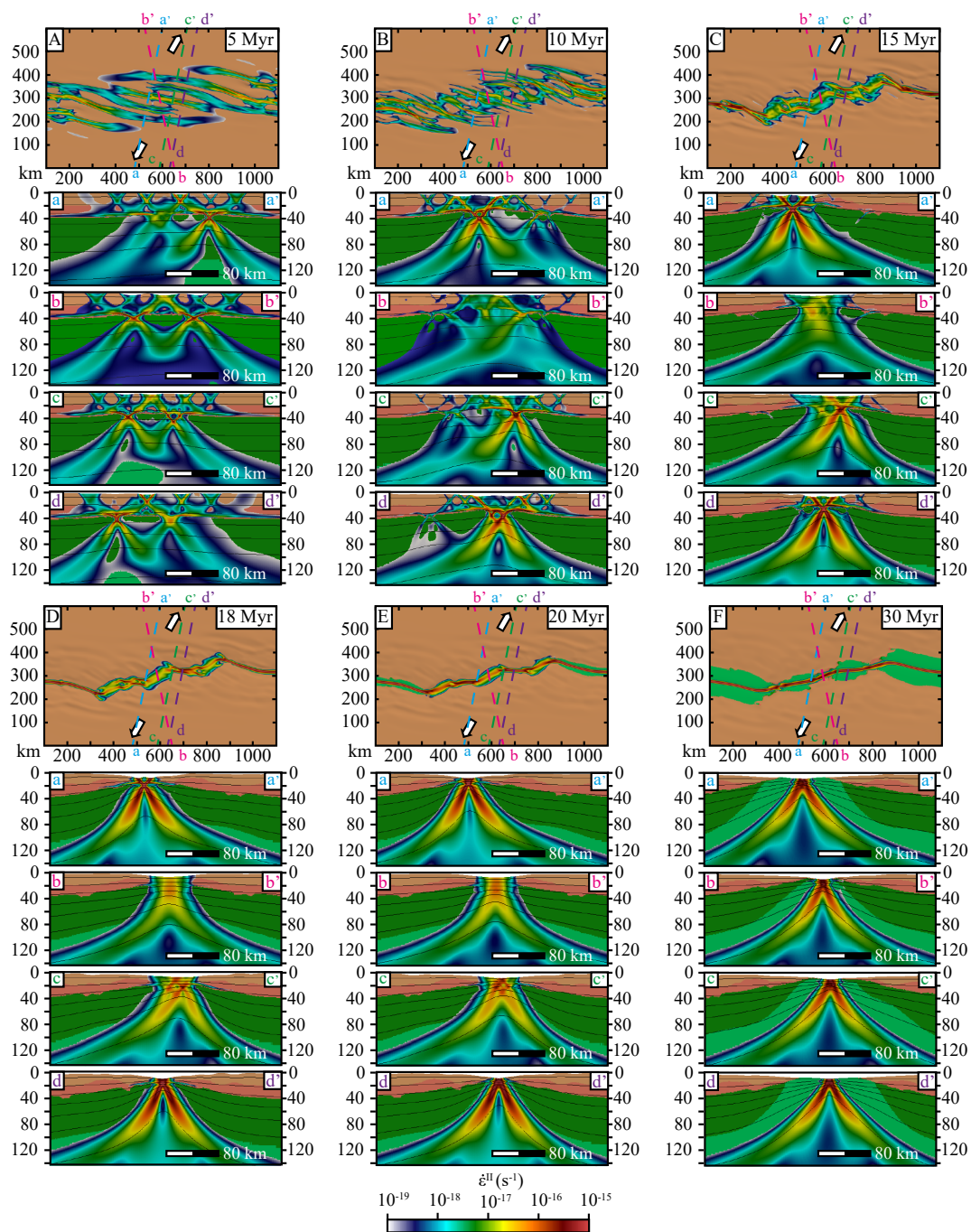




(Figure 5)

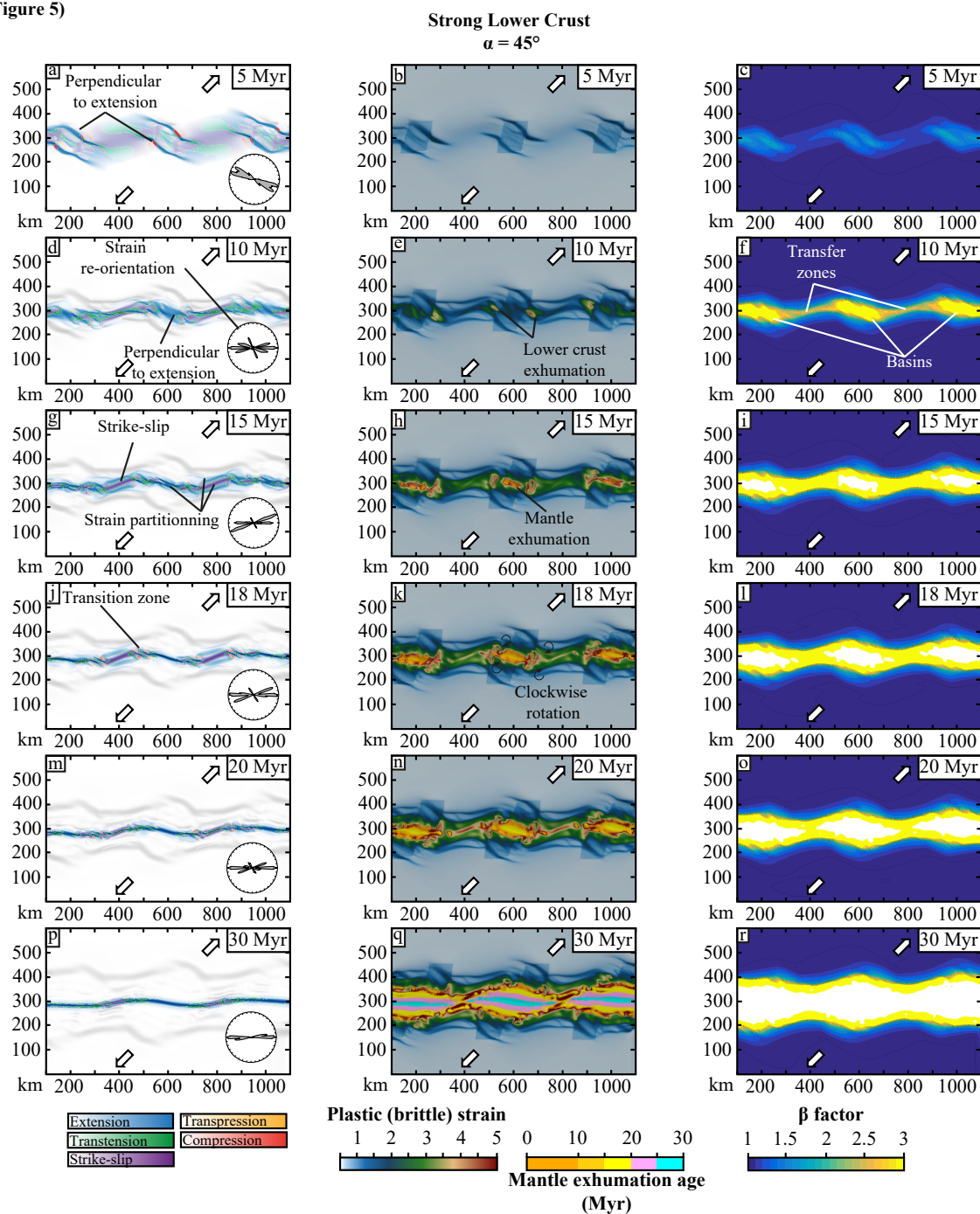




(Figure 6)

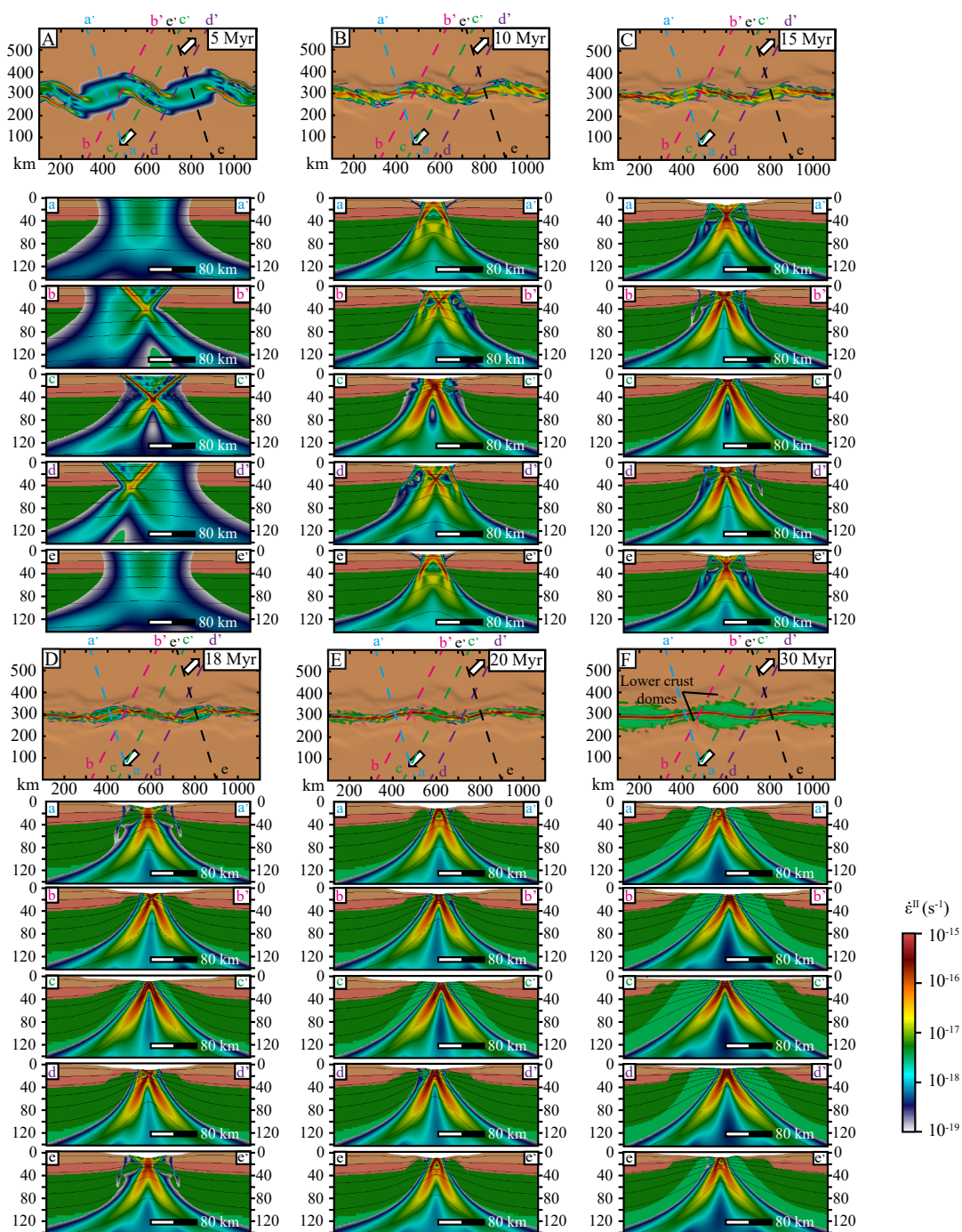




(Figure 7)

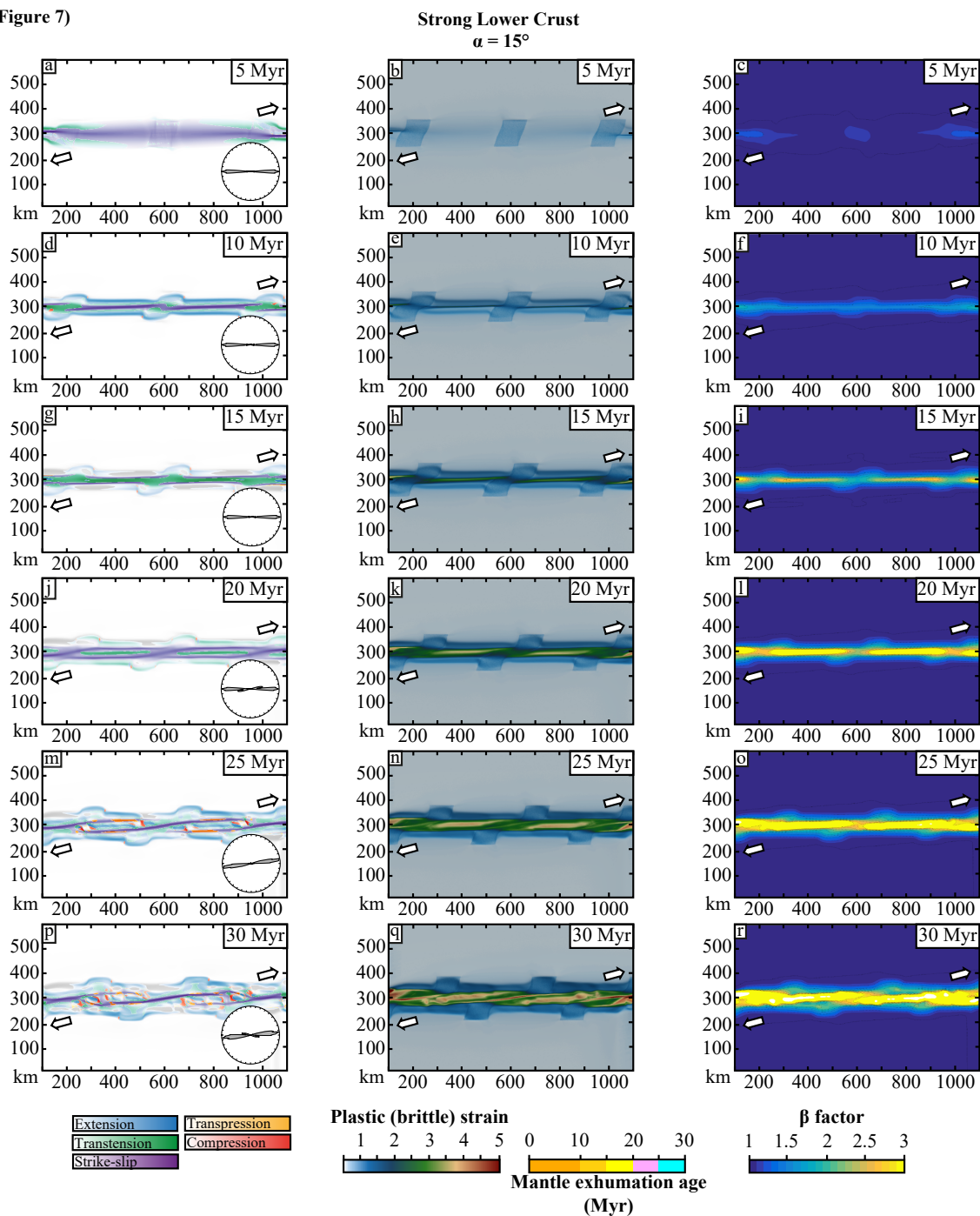




(Figure 8)

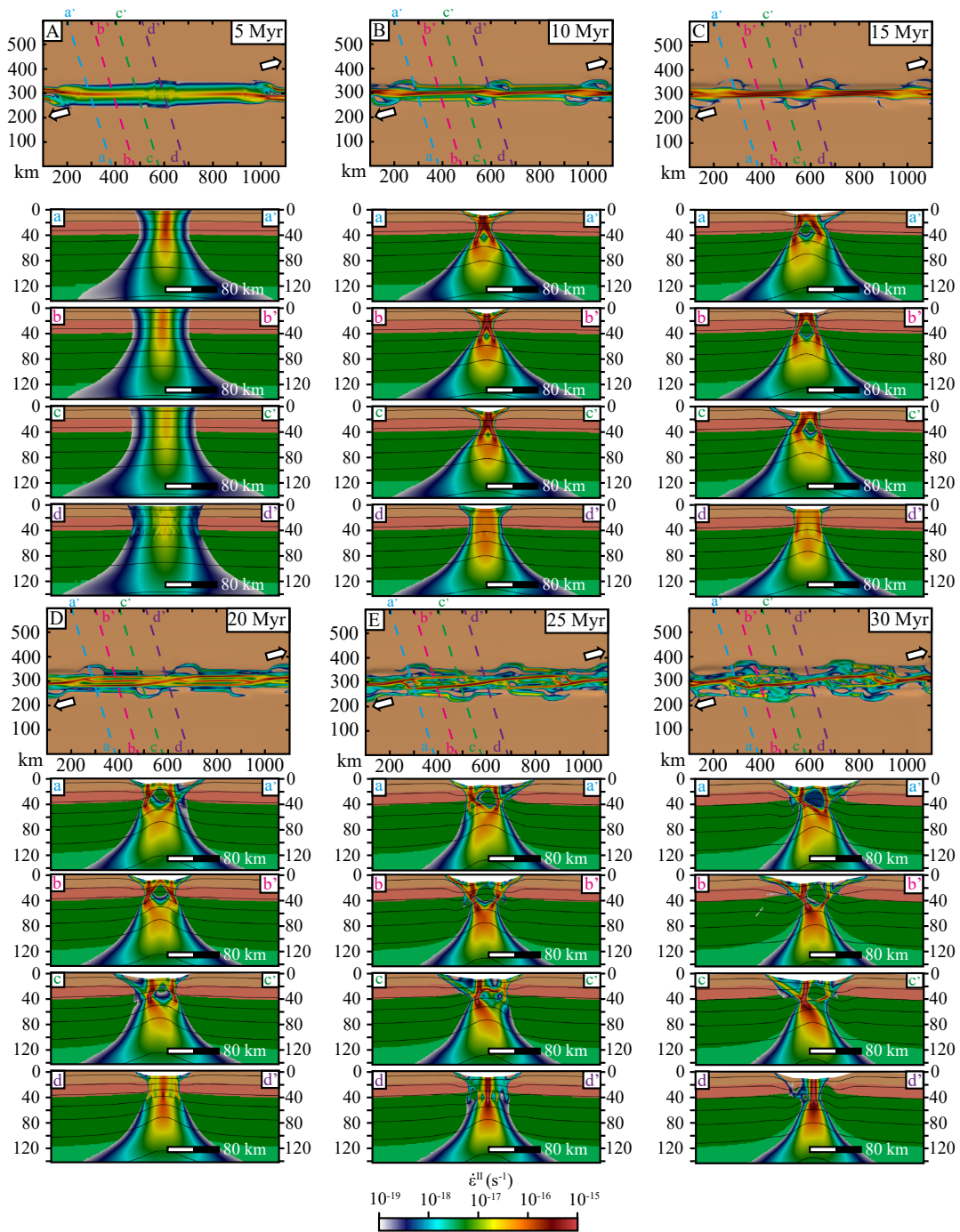




(Figure 9)

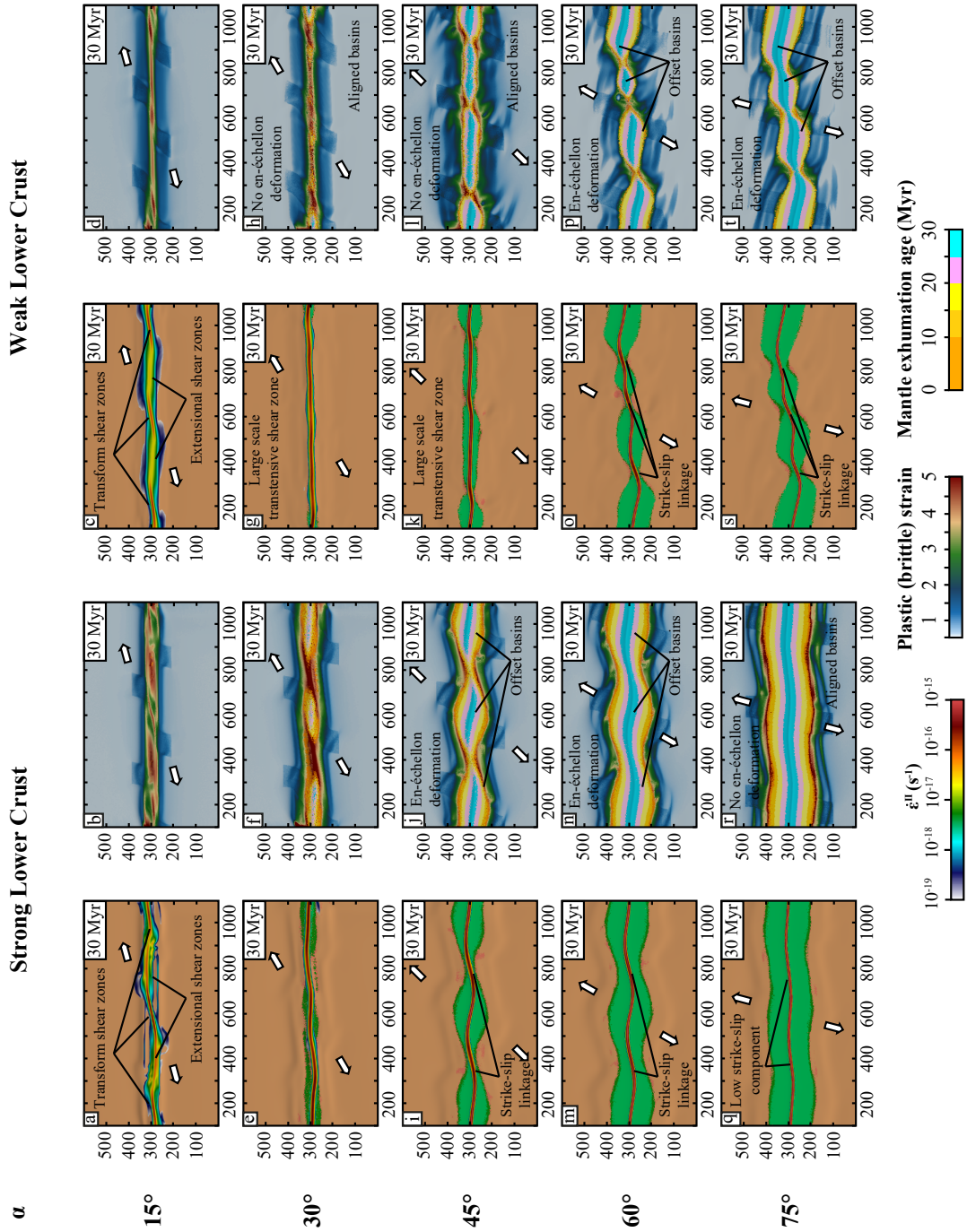




(Figure 10)

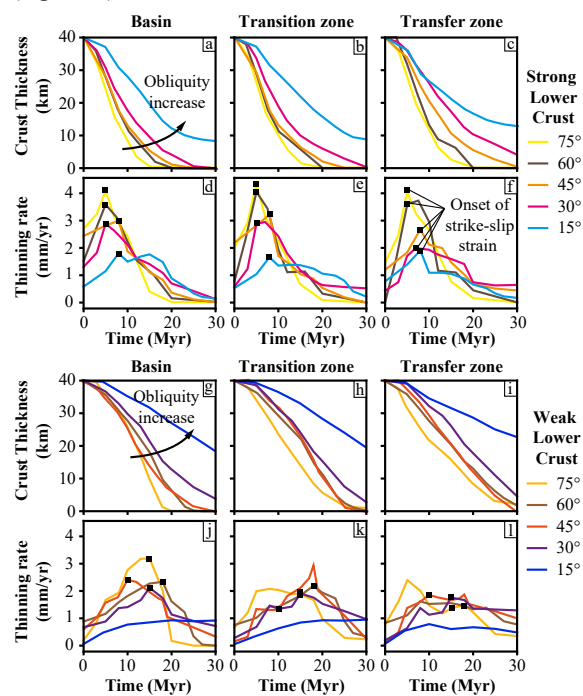




(Figure 11)

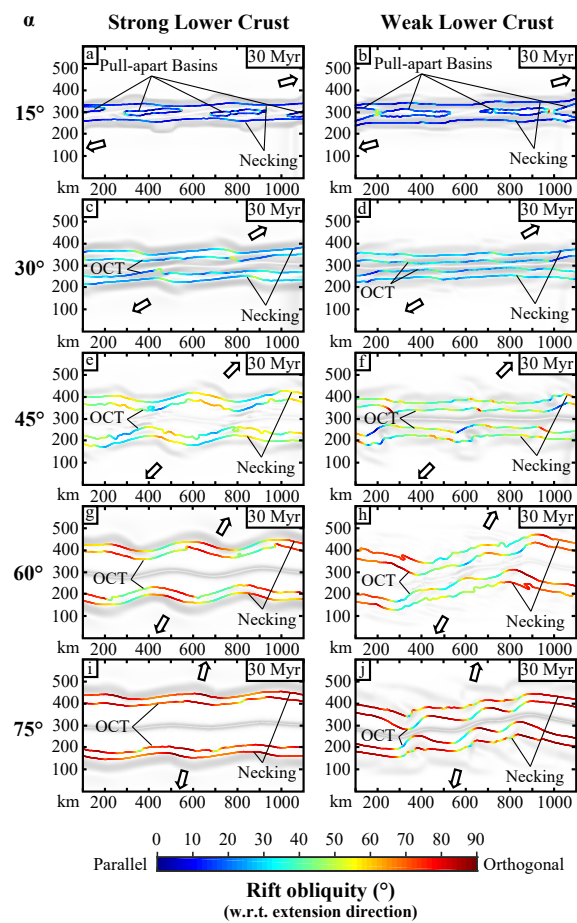




(Figure 12)

